Available online at www.sciencedirect.com
ScienceDirect
Comput. Methods Appl. Mech. Engrg. 400 (2022) 115467
Computer methods in applied mechanics and engineering
www.elsevier.com/locate/cma

A thermodynamically consistent finite strain phase field approach to ductile fracture considering multi-axial stress states

Sina Abrari Vajari[a], Matthias Neuner[a], Prajwal Kammardi Arunachala[a], Andy Ziccarelli[b], Gregory Deierlein[a], Christian Linder[a,*]

[a] Department of Civil and Environmental Engineering, Stanford University, Stanford, CA, USA
[b] Department of Civil, Construction, and Environmental Engineering, North Carolina State University, Raleigh, NC, USA

Received 22 May 2022; received in revised form 22 July 2022; accepted 23 July 2022
Available online 22 August 2022

Abstract

Phase field models for ductile fracture have gained significant attention in the last two decades due to their ability in implicitly tracking the nucleation and propagation of cracks. However, most crack phase field formulations for elastoplastic solids focus only on the effects of plastic deformation, and do not consider the different multi-axial stress states that may arise in practical designs. In this work, a thermodynamically consistent phase field approach coupled with finite strain plasticity, considering multi-axial stress states is presented. In order to account for the coupling between plasticity and stress states, the Stress-Weighted Ductile Fracture Model (SWDFM) is utilized. The SWDFM represents a criterion for predicting ductile crack initiation under both monotonic and cyclic loadings based on histories of an internal plastic variable, stress triaxiality, and the Lode angle parameter. The excellent performance of the SWDFM for predicting ductile crack initiation motivates for its incorporation into a phase field approach for predicting both crack initiation and propagation through degradation of the fracture toughness. Moreover, based on the second law of thermodynamics, exact requirements are imposed on the rate at which the fracture toughness can evolve. A novel function for degrading the plastic yield surface during the evolution of damage is introduced. This function, in line with experimental observations, leads to an accumulation of plastic deformation in damaged regions of a solid, and avoids numerical instabilities arising from concentrations of large plastic deformations in severely damaged regions. For validating the proposed model, results of computational simulations are compared to data from selected tests considering different multi-axial stress states. Comparisons of the numerical results with data from laboratory experiments demonstrate the capabilities of the proposed framework.

Keywords: Phase field fracture; Ductile fracture; Finite strain plasticity; Stress triaxiality; Lode angle

---

1. Introduction

Ductile fracture in solids is one of the most common failure mechanisms, and its study is of great importance in engineering applications for predicting the load capacity, and for preventing crack-induced failure. The investigation of fracture dates back to the seminal work of Griffith [1] studying brittle fracture of materials, who stated that a

---

* Corresponding author.
E-mail address: linder@stanford.edu (C. Linder).

https://doi.org/10.1016/j.cma.2022.115467
0045-7825/

crack originates in a solid when the amount of stored strain energy reaches a critical value known as the energy release rate or fracture toughness, reflecting the amount of energy required to create a unit area of crack surface. Unlike brittle fracture, which usually occurs abruptly and at small deformations, ductile fracture exhibits a more involved behavior before cracking such as considerable plastic dissipation, hardening, and necking, which causes failure to occur at relatively large strains. As a result, the prediction of failure mechanisms due to crack initiation and propagation in elastoplastic solids is a challenging task.

Among many methods, the phase field approach to fracture, a smeared crack modeling technique, has gained significant attention in the last two decades. The phase field approach originated in the mechanics community based on a variational formulation of brittle fracture by Francfort and Marigo [2], and was later employed for numerical solutions by Bourdin et al. [3]. The phase field approach implicitly tracks the propagation of a crack through the evolution of an order parameter (the crack phase field) that transitions smoothly between sound and fully cracked material points. As a result, unlike for discrete crack models where displacement jumps are introduced in the kinematical description [4–9], the tedious task of tracking the crack surface is avoided.

Following the concepts of fracture mechanics, Miehe et al. [10,11] proposed a gradient damage theory based on a geometrical approximation of the crack surface, leading to a thermodynamically consistent approach to phase field fracture combined with an irreversibility constraint for the order parameter. In addition, Miehe et al. [11], based on the spectral decomposition of the strain tensor, introduced a mechanism for distinguishing crack response under tensile and compressive forces. To capture an asymmetric fracture response in tension and compression and to avoid crack interpenetration, Amor et al. [12] also used a form of spherical and deviatoric decomposition of the strain energy. Borden et al. [13], Bourdin et al. [14], Remacle et al. [15], and Geelen et al. [16] extended the phase field model to represent fracture in dynamic conditions, and they showed its capability in modeling crack branching without a need for ad hoc criteria. Miehe and Schänzel [17], Talamini et al. [18], and Swamynathan et al. [19] outlined a phase field framework for modeling fracture in polymers. Phase field models for brittle fracture of shells were proposed by Reinoso et al. [20] and Kiendl et al. [21]. To study the failure mechanism of geological materials, Choo and Sun [22] suggested a phase field model considering the effects of confining pressure and strain rate, and Zhou et al. [23] presented a new formulation for compressive-shear fracture in brittle rock-like materials. Multi-physics phase field formulations were proposed by Zhang et al. [24] for modeling fracture in silicon electrodes, and by Cheng et al. [25] for capturing crack patterns induced by thermal spalling in concrete. Recently, Wu et al. [26] provided an extensive overview of the available phase field formulations for fracture in both quasi-static and dynamic conditions.

For modeling ductile fracture, different phase field frameworks for elastoplastic materials have been proposed. Borden et al. [27] developed a finite strain ductile phase field formulation based on micro-force balance laws. In their formulation, the plastic yield surface is degraded with the ongoing evolution of fracture, leading to an accumulation of plastic deformation while avoiding nonphysical elastic deformation in damaged regions of a solid. Furthermore, in order to avoid damage accumulation at small plastic deformations, they assumed that the plastic strain energy acts as an additional crack driving force once it exceeds a threshold value. Most recently, Li et al. [28] revisited the same concept. However, in their formulation the energy threshold value is not constant, rather it evolves with the stress and strain state inside the body. Ambati et al. [29,30] related the evolution of fracture to plasticity by degrading the toughness of material points exhibiting large plastic deformations, a concept that is in line with experimental observations. Yin and Kaliske [31] associated the growth of damage to the evolution of a plastic strain measure, assuming that the local fracture toughness decreases due to increasing plastic deformations. A similar concept was also extended to the geometrically nonlinear setting by Han et al. [32], where in addition to the degradation of the fracture toughness, the plastic strain energy drives the evolution of cracks. Recently, Alessi et al. [33] compared selected available ductile phase field models and investigated the coupling between plasticity and the phase field evolution.

For many materials exhibiting ductile fracture, the occurring large deformations as well as the localization of deformations invalidate the assumption of the small strain theory. Hence, the proper kinematical description of deformations demands for a formulation in the geometrical exact regime. However, compared to formulations in the small strain regime, few approaches for ductile phase field fracture under finite deformation have been proposed. As pointed out, Ambati et al. [30], Borden et al. [27], and Han et al. [32] have extended the ductile phase field framework to a finite deformation setting. Furthermore, Miehe et al. [34] incorporated a thermodynamically consistent framework of ductile phase field fracture into a formulation of gradient thermo-plasticity in the finite deformation regime. In their work, the crack driving forces are based on the mass specific elastic and plastic works, and barrier functions are defined to hinder the evolution of damage at low levels of elastic and plastic deformations. Aldakheel et al. [35] combined an elastoplastic constitutive model for porous media with a phase field approach for finite strain deformations, and showed the capabilities of the proposed method in capturing experimentally observed cup-cone failure mechanisms.

It is well understood that ductile fracture in elastoplastic materials, especially in metals, happens at micro-level where nucleation of small defects such as micro-cracks and micro-voids, concentrated mostly in regions with large plastic deformations, initiates the crack formation. Micro-voids grow and coalesce to form larger voids, and consequently realize their effects at the macro-scale, leading to a loss of stiffness and finally rupture [36,37]. In addition to the amount of plastic deformation, the mechanism of micro-void growth is affected to a great extent by the multi-axial stress state inside the body. McClintock [38] and Rice and Tracey [39] highlighted the influence of the hydrostatic stress component on the ductile behavior of metals through theoretical studies of growth of voids embedded in plastically deforming solids. Following a continuum damage model, Lemaitre [40] and La Rosa et al. [41] observed that fracture criteria should depend on the hydrostatic stress. Experiments done by Norris et al. [42], Oyane et al. [43], and Bao and Wierzbicki [44] also indicated the critical importance of the level of hydrostatic stress in changing the mechanism of fracture. Accordingly, in order to accurately capture the ductile fracture of materials, models should consider a coupling between the macroscopic stress state, the plastic deformation, and the evolution of damage. However, in contrast to these findings, except for a few models [27,28,35,45], most ductile phase field formulations focus only on the effects of plastic deformation, while they do not consider different multi-axial stress states that may arise in practical designs.

On the other hand, independently of phase field crack developments, many continuum ductile fracture models provide an estimate for the local initiation of fracture by linking the damage evolution to both plasticity and the stress state [46–49]. In these models, a damage field variable calculated based on the stress and strain histories counts towards the inception of cracks. Johnson and Cook [50] introduced a damage model depending on the strain rate, the temperature, and the pressure, and they concluded that fracture is heavily influenced by the hydrostatic pressure compared to the other two factors. Following the work of Gurson [51], Tvergaard and Needleman [36] proposed a model coupling the evolution of damage to plasticity and the stress state through void growth. Despite offering a connection between the evolution of damage, plasticity and the stress intensity, most of the prior studies were concerned with a limited range of the stress and strain states, and loading conditions. To overcome this shortcoming, most recently and based on previous work of Smith et al. [52], the Stress-Weighted Ductile Fracture Model (SWDFM) [53] was proposed. The SWDFM represents a criterion for predicting ductile crack initiation based on the mechanism of micro-void growth and coalescence under both monotonic and cyclic loadings. In this model, a damage quantity, which is calculated based on histories of plastic strain and stress, signals the inception of fracture once its value attains a critical limit. Unlike prior continuum damage models, the SWDFM was validated against experimental results with large plastic strains, considering multi-axial stress conditions [53,54].

The excellent performance of the SWDFM for predicting ductile crack initiation alongside its micro-mechanically based formulation motivates for a combination with the phase field method for predicting the propagation of cracks. This is the focus of this work. We present a phase field approach to ductile fracture based on the SWDFM accounting for different types of multi-axial stress states and large inelastic deformations, formulated in a geometrically exact setting. To this end, we follow a micro-mechanically motivated approach, deriving all governing equations from micro-force balance laws alongside the first and second laws of thermodynamics within the finite strain regime. The SWDFM initiation criterion is incorporated into the model for predicting both crack initiation and propagation through the degradation of the resistance to ductile fracture in line with previous studies [31,32,55,56]. From the second law of thermodynamics, and based on the dissipation inequality, restrictions are imposed on the rate at which the fracture toughness can evolve.

We start our investigation in Section 2, describing the finite strain kinematics, the phase field approximation to fracture, and the derivation of the balance laws of the governing equations in terms of a general potential functional. The hyperelastic–plastic constitutive model specific to this work, governing the stress and the fracture responses of a solid, is presented in Section 3. The degradation of the fracture toughness, and its coupling to the SWDFM are also investigated in this Section. The strong and weak forms of the governing equations and the finite element implementation are shown in Section 4. Section 5 contains a representative numerical study of tests considering different multi-axial stress states, including a comparison of the numerical results with data from real world experiments. Finally, Section 6 concludes with a summary.

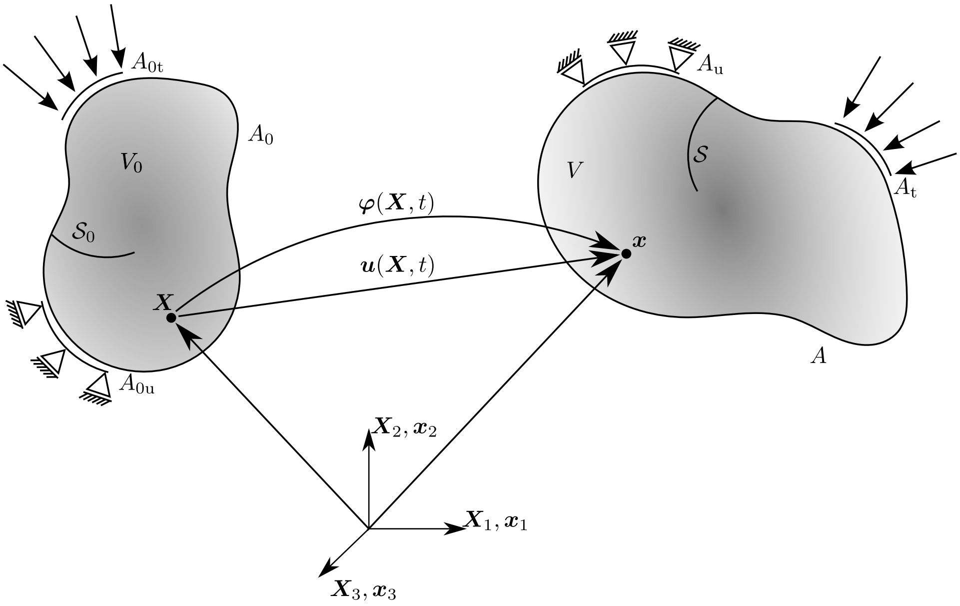

Fig. 1. Finite deformation of a solid with a discontinuity. The body at time $t \subset \mathbb{R}^+$ undergoes a deformation $\varphi(\boldsymbol{X}, t)$, which maps the reference material point $\boldsymbol{X} \in V_0$, onto the current material point $\boldsymbol{x} \in V$ such that $\boldsymbol{x} = \varphi(\boldsymbol{X}, t)$.

2. Framework

2.1. Finite strain kinematics

The reference configuration of a body of interest with an internal discontinuity boundary $\mathcal{S}_0$ is denoted by $V_0 \subset \mathbb{R}^{\mathrm{nd}}$ and its surface with $A_0 \subset \mathbb{R}^{\mathrm{nd}-1}$, with nd $\in \{2, 3\}$ as the spatial dimension. The corresponding current configuration is shown by $V \subset \mathbb{R}^{\mathrm{nd}}$ with the discontinuity $\mathcal{S}$ and surface $A \subset \mathbb{R}^{\mathrm{nd}-1}$. The position vectors at the reference and current configurations are denoted by $\boldsymbol{X}$ and $\boldsymbol{x}$, respectively. The body in time interval of $[0, t] \subset \mathbb{R}^+$ undergoes a deformation $\varphi(\boldsymbol{X}, t) : V_0 \times [0, t] \rightarrow \mathbb{R}^{\mathrm{nd}}$, which maps the reference material points ($\boldsymbol{X} \in V_0$) onto the current material points ($\boldsymbol{x} \in V$) such that $\boldsymbol{x} = \varphi(\boldsymbol{X}, t)$, as visualized in Fig. 1. We denote derivatives with respect to the reference frame as

$$(\bullet)_{,X} = \frac{\partial}{\partial \boldsymbol{X}}(\bullet) \quad \text{and} \quad \mathrm{Div}(\bullet) = \frac{\partial}{\partial \boldsymbol{X}} \cdot (\bullet), \tag{1}$$

and derivatives with respect to the coordinates in the spatial configuration as

$$(\bullet)_{,\boldsymbol{x}} = \frac{\partial}{\partial \boldsymbol{x}}(\bullet) \quad \text{and} \quad \mathrm{div}(\bullet) = \frac{\partial}{\partial \boldsymbol{x}} \cdot (\bullet). \tag{2}$$

Furthermore, $\frac{\mathrm{d}}{\mathrm{d}t}(\bullet) = (\dot{\bullet})$ denotes the material time derivative. We also recall the definition of the deformation gradient as $\boldsymbol{F} := \varphi_{,X}(\boldsymbol{X}, t)$, with its determinant $J := \det(\boldsymbol{F}) > 0$ known as the Jacobian of transformation. Furthermore, for an elastoplastic response we assume the existence of an intermediate, in general incompatible, stress-free configuration, which leads to a local multiplicative decomposition of the deformation gradient [57,58] into an elastic $\boldsymbol{F}^{\mathrm{e}}$ part and a plastic $\boldsymbol{F}^{\mathrm{p}}$ part as

$$\boldsymbol{F} = \boldsymbol{F}^{\mathrm{e}} \boldsymbol{F}^{\mathrm{p}}. \tag{3}$$

We define the elastic Eulerian logarithmic strain tensor

$$\boldsymbol{\varepsilon}^{\mathrm{e}} = \tfrac{1}{2} \ln\left(\boldsymbol{b}^{\mathrm{e}}\right). \tag{4}$$

In this equation, $\boldsymbol{b}^{\mathrm{e}} = \boldsymbol{F}^{\mathrm{e}} \boldsymbol{F}^{\mathrm{eT}}$ is the elastic left Cauchy–Green strain tensor, whose Lie derivative is defined as

$$\mathcal{L}_v \boldsymbol{b}^{\mathrm{e}} = \dot{\boldsymbol{b}}^{\mathrm{e}} - \boldsymbol{l} \boldsymbol{b}^{\mathrm{e}} - \boldsymbol{b}^{\mathrm{e}} \boldsymbol{l}^{\mathrm{T}} \tag{5}$$

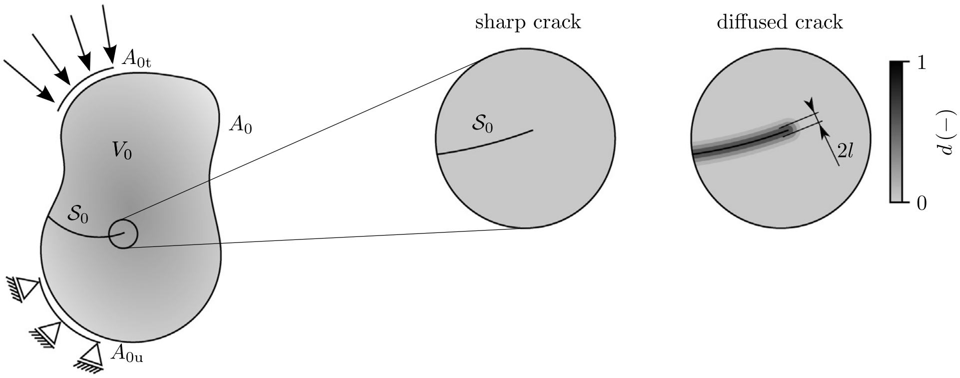

Fig. 2. Reference configuration of a solid with a sharp crack surface $\mathcal{S}_0$, and its regularized approximation using the phase field parameter d. The length scale parameter l controls the length over which the crack is diffused.

with the help of the spatial velocity gradient $\boldsymbol{l} = \dot{\boldsymbol{F}}\boldsymbol{F}^{-1}$. Furthermore, we decompose $\boldsymbol{l}$ into its symmetric and skew-symmetric parts as

$$\boldsymbol{D} = \mathrm{sym}(\boldsymbol{l}) = \tfrac{1}{2}\left(\boldsymbol{l} + \boldsymbol{l}^{\mathrm{T}}\right) \quad \text{and} \quad \boldsymbol{\omega} = \mathrm{skew}(\boldsymbol{l}) = \tfrac{1}{2}\left(\boldsymbol{l} - \boldsymbol{l}^{\mathrm{T}}\right), \tag{6}$$

with $\boldsymbol{D}$ denoting the rate of deformation tensor, and $\boldsymbol{\omega}$ denoting the spin tensor.

We describe the behavior of the fracturing solid by the displacement field $\boldsymbol{u} := \boldsymbol{x} - \boldsymbol{X}$ defined on the set

$$\boldsymbol{u}(\boldsymbol{X}) \in \left\{\boldsymbol{u} \mid \boldsymbol{u}(\boldsymbol{X}) = \bar{\boldsymbol{u}}\, \forall \boldsymbol{X} \in A_{0\mathrm{u}}\right\}. \tag{7}$$

The surface A_0 is decomposed into $A_{0\mathrm{u}}$ and $A_{0\mathrm{t}}$, where the displacement field satisfies the Dirichlet boundary conditions on $A_{0\mathrm{u}}$ with given values of $\bar{\boldsymbol{u}}$, and the Neumann-type boundary conditions defined over $A_{0\mathrm{t}}$ with prescribed values of the traction. Dirichlet and Neumann boundary conditions are also defined over A_{u} and A_{t} in the deformed configuration as depicted in Fig. 1.

2.2. Phase field approximation

To study the evolution of a crack inside a solid, we introduce the time-dependent crack phase field d, illustrated in Fig. 2, which distinguishes between an intact ($d = 0$) versus a fully damaged ($d = 1$) material point and is defined on the set

$$d(\boldsymbol{X}) \in \left\{d \mid d(\boldsymbol{X}) \in [0,1],\ \dot{d}(\boldsymbol{X}) \geq 0\, \forall \boldsymbol{X} \in V_0\right\}. \tag{8}$$

The condition $\dot{d}(\boldsymbol{X}) \geq 0$ follows physical considerations, and it guarantees that internal discontinuities evolve in an irreversible manner [11]. Accounting for reversibility might be required under special circumstances such as cyclic loadings or for brittle materials that can retain their full strength even after experiencing loads close to failure limits [59]. However, since in this initial study we are concerned with ductile behavior of materials under monotonic loadings, the crack irreversibility is a logical assumption.

Next, following [60] we approximate the energy required to create a diffusive fracture surface as

$$\int_{\mathcal{S}_0} G_c \,\mathrm{d}\mathcal{S}_0 \approx \int_{V_0} G_c \gamma \,\mathrm{d}V_0 \tag{9}$$

with the help of G_c the critical fracture energy per unit area in the reference configuration. Moreover, the crack surface density per unit reference volume function γ [10,11], depending on the crack phase field and its gradient, is defined as

$$\gamma(d, d_{,\boldsymbol{X}}; l) = \frac{1}{c_0}\left(\frac{1}{l}\Gamma(d) + l d_{,\boldsymbol{X}} \cdot d_{,\boldsymbol{X}}\right). \tag{10}$$

Therein, $\Gamma(d)$ is the geometric crack function, which characterizes the homogeneous and local evolution of the crack phase field [61], and l is a regularization parameter, known as the phase field length scale parameter which controls the diffusive crack width. Furthermore, $c_0 = 4\int_0^1 \sqrt{\Gamma(\hat{d})}\,\mathrm{d}\hat{d}$ is the scaling parameter introduced such that the sharp crack surface is recovered for a vanishing length scale parameter, i.e.,

$$\lim_{l\to 0}\int_{V_0} G_c\gamma\,\mathrm{d}V_0 = \int_{\mathcal{S}_0} G_c\,\mathrm{d}\mathcal{S}_0. \tag{11}$$

In this work, we follow the geometrical approximation of a crack surface shown in [10] and assume a crack surface density function in the form

$$\gamma(d, d_{,X}; l) = \tfrac{1}{2}\left(\frac{1}{l}d^2 + l d_{,X}\cdot d_{,X}\right). \tag{12}$$

As shown later on, this definition of the crack surface density leads to a strong form of the governing equation involving second-order derivatives of d. Hence, models employing this form of γ are known as *second-order* phase field theories [62].

2.3. Balance laws

Since the process of material degradation is governed by physical mechanisms at the micro level, where micro-forces cause the evolution of micro-voids, we formulate the (quasi-static) balance laws for micro-forces alongside the first and second laws of thermodynamics following [63,64]. We start with the balance laws derived in the reference configuration V_0 with boundary A_0. The derivation of these laws in the deformed configuration V can be done in a similar manner. It is worth mentioning that although the equations are derived over V_0, they can also be derived for any subset $\mathcal{P}_0 \subset V_0$, as shown in [27].

Balance of mass. Assuming that mass of the system is conserved at all times, the balance of mass in its local form in the reference configuration is

$$\dot{\rho}_0 = 0 \quad \text{in } V_0. \tag{13}$$

Therein, ρ_0 is the mass density per unit reference volume. Defining $\rho := J^{-1}\rho_0$ as the mass density per unit current volume, the local balance of mass in the current configuration is stated as

$$\dot{\rho} + \rho\,\mathrm{div}(\dot{\boldsymbol{u}}) = 0 \quad \text{in } V. \tag{14}$$

Balance of linear momentum. The balance of linear momentum in the reference configuration is written as

$$\frac{\mathrm{d}}{\mathrm{d}t}\int_{V_0}\rho_0\dot{\boldsymbol{u}}\,\mathrm{d}V_0 = \int_{V_0}\boldsymbol{B}\,\mathrm{d}V_0 + \int_{A_0}\boldsymbol{T}_{\mathrm{N}}\,\mathrm{d}A_0 \to \mathrm{Div}(\boldsymbol{P}) + \boldsymbol{B} = \rho_0\ddot{\boldsymbol{u}} \quad \text{in } V_0, \tag{15}$$

with $\boldsymbol{T}_{\mathrm{N}} = \boldsymbol{P}\boldsymbol{N}$ denoting the traction force acting on the surface of the reference configuration. In this equation, $\boldsymbol{P}$ is the first Piola–Kirchhoff stress tensor, $\boldsymbol{N}$ is the outward unit normal vector at the boundary of the reference configuration, and $\boldsymbol{B}$ is the body force per unit volume of the reference configuration. Writing the equation in the current configuration, the local form leads to

$$\mathrm{div}(\boldsymbol{\sigma}) + J^{-1}\boldsymbol{B} = \rho\ddot{\boldsymbol{u}} \quad \text{in } V \tag{16}$$

with $\boldsymbol{\sigma} = \frac{1}{J}\boldsymbol{P}\boldsymbol{F}^{\mathrm{T}}$ denoting the Cauchy stress tensor.

Balance of angular momentum. The balance of momentum of momentum in the reference configuration is expressed as

$$\frac{\mathrm{d}}{\mathrm{d}t}\int_{V_0}\boldsymbol{X}\times\rho_0\dot{\boldsymbol{u}}\,\mathrm{d}V_0 = \int_{V_0}\boldsymbol{X}\times\boldsymbol{B}\,\mathrm{d}V_0 + \int_{A_0}\boldsymbol{X}\times\boldsymbol{P}\boldsymbol{N}\,\mathrm{d}A_0 \to \boldsymbol{P}\boldsymbol{F}^{\mathrm{T}} = \boldsymbol{F}\boldsymbol{P}^{\mathrm{T}} \quad \text{in } V_0. \tag{17}$$

Similarly, the balance of angular momentum in the deformed configuration leads to the symmetry of the Cauchy stress tensors, i.e.,

$$\boldsymbol{\sigma} = \boldsymbol{\sigma}^{\mathrm{T}} \quad \text{in } V. \tag{18}$$

Micro-force balance law. For the micro-force balance law, we assume that the phase field is characterized by an intrinsic micro-force $\pi(\boldsymbol{X}, t)$, and an extrinsic micro-force acting on the body $h(\boldsymbol{X}, t)$. Furthermore, we assume the existence of a micro-force traction vector $\boldsymbol{\xi}(\boldsymbol{X}, t)$, such that $\boldsymbol{\xi} \cdot \boldsymbol{N}$ is the external micro-force acting on the surface of the body A_0. We then get the micro-force balance law in the reference configuration as

$$\int_{A_0} \boldsymbol{\xi} \cdot \boldsymbol{N} \,\mathrm{d}A_0 + \int_{V_0} h \,\mathrm{d}V_0 + \int_{V_0} \pi \,\mathrm{d}V_0 = 0 \rightarrow \mathrm{Div}\boldsymbol{\xi} + h + \pi = 0 \quad \text{in } V_0. \tag{19}$$

First law of thermodynamics. Restricting the discussion to the adiabatic and isothermal case, the energy balance is written as

$$\frac{\mathrm{d}}{\mathrm{d}t} \int_{V_0} \left(\tfrac{1}{2}\rho_0 \dot{\boldsymbol{u}} \cdot \dot{\boldsymbol{u}} + \rho_0 e_0\right) \mathrm{d}V_0 = \int_{V_0} \boldsymbol{B} \cdot \dot{\boldsymbol{u}} \,\mathrm{d}V_0 + \int_{A_0} \boldsymbol{P}\boldsymbol{N} \cdot \dot{\boldsymbol{u}} \,\mathrm{d}A_0 + \int_{A_0} (\boldsymbol{\xi} \cdot \boldsymbol{N})\dot{d} \,\mathrm{d}A_0 + \int_{V_0} h\dot{d} \,\mathrm{d}V_0 \,, \tag{20}$$

with e_0 denoting the internal energy per unit reference mass and $\dot{d}$ as the rate-of-work conjugate to the micro-forces. Complementing this equation with (13), (15), (17), (19), and by using the divergence theorem for the boundary terms, the equation in the reference configuration is transformed to

$$\int_{V_0} \rho_0 \dot{e}_0 \,\mathrm{d}V_0 = \int_{V_0} \boldsymbol{P} : \dot{\boldsymbol{F}} \,\mathrm{d}V_0 + \int_{V_0} \boldsymbol{\xi} \cdot \dot{d}_{,\boldsymbol{X}} \,\mathrm{d}V_0 - \int_{V_0} \pi \dot{d} \,\mathrm{d}V_0 \tag{21}$$

which in the local form becomes

$$\rho_0 \dot{e}_0 = \boldsymbol{P} : \dot{\boldsymbol{F}} + \boldsymbol{\xi} \cdot \dot{d}_{,\boldsymbol{X}} - \pi \dot{d} \quad \text{in } V_0. \tag{22}$$

Second law of thermodynamics. With θ as the absolute temperature of the system, s_0 the referential entropy per unit mass, r the heat source per unit reference mass, and $\boldsymbol{q}$ the heat flux in the reference configuration, the second law of thermodynamics is stated as

$$\frac{\mathrm{d}}{\mathrm{d}t} \int_{V_0} \rho_0 s_0 \,\mathrm{d}V_0 \geq \int_{V_0} \frac{\rho_0 r}{\theta} \,\mathrm{d}V_0 - \int_{A_0} \frac{\boldsymbol{q} \cdot \boldsymbol{N}}{\theta} \,\mathrm{d}A_0 \,, \tag{23}$$

where again by using the divergence theorem for the boundary term the local form follows as

$$\rho_0 \dot{s}_0 \theta \geq \rho_0 r - \mathrm{Div}\boldsymbol{q} + \frac{\boldsymbol{q} \cdot \theta_{,\boldsymbol{X}}}{\theta} \quad \text{in } V_0. \tag{24}$$

For isothermal and adiabatic processes, i.e., assuming $r = 0$, $\boldsymbol{q} = \boldsymbol{0}$, and $\theta_{,\boldsymbol{X}} = \boldsymbol{0}$, the local form of the second law transforms into

$$\rho_0 \dot{s}_0 \theta \geq 0 \quad \text{in } V_0. \tag{25}$$

Next, the Helmholtz free energy ψ is introduced by means of the Legendre-transformation

$$e_0 := \psi + \theta s_0. \tag{26}$$

Taking $\dot{\theta} = 0$ and putting (26) back into (25), while utilizing (22), we get to

$$\boldsymbol{P} : \dot{\boldsymbol{F}} + \boldsymbol{\xi} \cdot \dot{d}_{,\boldsymbol{X}} - \pi \dot{d} - \rho_0 \dot{\psi} \geq 0 \quad \text{in } V_0 \,, \tag{27}$$

which can be similarly expressed as

$$\boldsymbol{\tau} : \boldsymbol{D} + \boldsymbol{\xi} \cdot \dot{d}_{,\boldsymbol{X}} - \pi \dot{d} - \rho_0 \dot{\psi} \geq 0 \quad \text{in } V_0 \tag{28}$$

in terms of the Kirchhoff stress tensor $\boldsymbol{\tau} = \boldsymbol{P}\boldsymbol{F}^{\mathrm{T}}$. We assume a stored energy functional of the form

$$\mathcal{E} = \int_{V_0} \Psi(\mathsf{c}) \,\mathrm{d}V_0 \tag{29}$$

with $\Psi(\mathsf{c}) = \rho_0 \psi(\mathsf{c})$. Here $\mathsf{c} := \{\boldsymbol{\varepsilon}^{\mathrm{e}}, \alpha, d, d_{,\boldsymbol{X}}, G_c\}$ is the set of constitutive state variables, with the Eulerian logarithmic strain tensor $\boldsymbol{\varepsilon}^{\mathrm{e}}$ as one of the state variables. As shown later on, this choice alongside the use of α as the scalar internal plastic variable is two-fold: First it allows for use of the well-established volumetric and deviatoric decomposition of the elastic strain energy, a concept that has been used widely in the small strain regime, and second, it facilitates a straightforward extension of small strain plasticity models to the finite strain regime. Finally, G_c is considered as a variable to reflect the evolution of the fracture toughness.

The material time derivative of the internal energy is obtained as

$$\rho_0 \dot{\psi}(\boldsymbol{\varepsilon}^{\mathrm{e}}, \alpha, d, d_{,\boldsymbol{X}}, G_c) = \dot{\Psi} = \frac{\partial \Psi}{\partial \boldsymbol{b}^{\mathrm{e}}} : \dot{\boldsymbol{b}}^{\mathrm{e}} + \frac{\partial \Psi}{\partial \alpha} \dot{\alpha} + \frac{\partial \Psi}{\partial d} \dot{d} + \frac{\partial \Psi}{\partial d_{,\boldsymbol{X}}} \cdot \dot{d}_{,\boldsymbol{X}} + \frac{\partial \Psi}{\partial G_c} \dot{G}_c. \tag{30}$$

Using (5) and after some simplifications, this time derivative reduces to

$$\dot{\Psi} = \frac{\partial \Psi}{\partial \boldsymbol{b}^{\mathrm{e}}} : \mathcal{L}_v \boldsymbol{b}^{\mathrm{e}} + 2\frac{\partial \Psi}{\partial \boldsymbol{b}^{\mathrm{e}}}\boldsymbol{b}^{\mathrm{e}} : \boldsymbol{l} + \frac{\partial \Psi}{\partial \alpha}\dot{\alpha} + \frac{\partial \Psi}{\partial d}\dot{d} + \frac{\partial \Psi}{\partial d_{,\boldsymbol{X}}} \cdot \dot{d}_{,\boldsymbol{X}} + \frac{\partial \Psi}{\partial G_c}\dot{G}_c. \tag{31}$$

Combination with (28) yields

$$(\boldsymbol{\tau} - 2\frac{\partial \Psi}{\partial \boldsymbol{b}^{\mathrm{e}}}\boldsymbol{b}^{\mathrm{e}}) : \boldsymbol{D} + (-\pi - \frac{\partial \Psi}{\partial d})\dot{d} + (\boldsymbol{\xi} - \frac{\partial \Psi}{\partial d_{,\boldsymbol{X}}}) \cdot \dot{d}_{,\boldsymbol{X}} - \frac{\partial \Psi}{\partial \boldsymbol{b}^{\mathrm{e}}} : \mathcal{L}_v \boldsymbol{b}^{\mathrm{e}} - \frac{\partial \Psi}{\partial \alpha}\dot{\alpha} - \frac{\partial \Psi}{\partial G_c}\dot{G}_c \geq 0\,, \tag{32}$$

and employing the Coleman–Noll procedure [65] results in

$$\boldsymbol{\tau} = 2\frac{\partial \Psi}{\partial \boldsymbol{b}^{\mathrm{e}}}\boldsymbol{b}^{\mathrm{e}}\,, \quad \pi = -\frac{\partial \Psi}{\partial d}\,, \quad \boldsymbol{\xi} = \frac{\partial \Psi}{\partial d_{,\boldsymbol{X}}}. \tag{33}$$

For the Kirchhoff stress, this reduces to (see [66] for reference)

$$\boldsymbol{\tau} = 2\frac{\partial \Psi}{\partial \boldsymbol{b}^{\mathrm{e}}}\boldsymbol{b}^{\mathrm{e}} = \frac{\partial \Psi}{\partial \boldsymbol{\varepsilon}^{\mathrm{e}}} : \frac{\partial \ln \boldsymbol{b}^{\mathrm{e}}}{\partial \boldsymbol{b}^{\mathrm{e}}}\boldsymbol{b}^{\mathrm{e}} = \frac{\partial \Psi}{\partial \boldsymbol{\varepsilon}^{\mathrm{e}}}. \tag{34}$$

With these equations, we define the reduced total dissipation functional as

$$\mathcal{D} := \mathcal{D}^{\mathrm{p}} - \frac{\partial \Psi}{\partial G_c}\dot{G}_c \geq 0. \tag{35}$$

In this equation, $\mathcal{D}^{\mathrm{p}}$ is the plastic dissipation defined as

$$\mathcal{D}^{\mathrm{p}} := -\frac{\partial \Psi}{\partial \boldsymbol{b}^{\mathrm{e}}} : \mathcal{L}_v \boldsymbol{b}^{\mathrm{e}} - \mathcal{A}\dot{\alpha} \tag{36}$$

where we have introduced the thermodynamical force $\mathcal{A} := \frac{\partial \Psi}{\partial \alpha}$ conjugate to α. After some straightforward manipulations, the plastic dissipation can be expressed in terms of the Kirchhoff stress as

$$\mathcal{D}^{\mathrm{p}} := \boldsymbol{\tau} : \left(-\tfrac{1}{2}\mathcal{L}_v \boldsymbol{b}^{\mathrm{e}}\right)(\boldsymbol{b}^{\mathrm{e}})^{-1} - \mathcal{A}\dot{\alpha}. \tag{37}$$

3. Constitutive relations

We propose the Helmholtz free energy function with a general form

$$\rho_0 \psi(\boldsymbol{\varepsilon}^{\mathrm{e}}, \alpha, d, d_{,\boldsymbol{X}}, G_c) = \Psi = g(d)\Psi^{\mathrm{e}}_{+}(\boldsymbol{\varepsilon}^{\mathrm{e}}) + \Psi^{\mathrm{e}}_{-}(\boldsymbol{\varepsilon}^{\mathrm{e}}) + \Psi^{\mathrm{p}}(\alpha) + \Psi^{\mathrm{f}}(d, d_{,\boldsymbol{X}}, G_c) \tag{38}$$

depending on the set of state variables $\mathsf{c} := \{\boldsymbol{\varepsilon}^{\mathrm{e}}, \alpha, d, d_{,\boldsymbol{X}}, G_c\}$. Therein, Ψ^{e}_{+} and Ψ^{e}_{-} are the positive and negative elastic strain energies following the volumetric and deviatoric decomposition of [12] defined to capture the asymmetric fracture response in tension and compression. In this work we use

$$\Psi^{\mathrm{e}}_{+}(\boldsymbol{\varepsilon}^{\mathrm{e}}) = \tfrac{1}{2}\kappa\langle \operatorname{tr}\boldsymbol{\varepsilon}^{\mathrm{e}}\rangle^2_{+} + \mu \boldsymbol{\varepsilon}^{\mathrm{e}}_{\mathrm{dev}} : \boldsymbol{\varepsilon}^{\mathrm{e}}_{\mathrm{dev}} \quad \text{and} \quad \Psi^{\mathrm{e}}_{-}(\boldsymbol{\varepsilon}^{\mathrm{e}}) = \tfrac{1}{2}\kappa\langle \operatorname{tr}\boldsymbol{\varepsilon}^{\mathrm{e}}\rangle^2_{-} \tag{39}$$

where the bulk modulus κ and the shear modulus μ are materials parameters related to the Young's modulus E, and the Poisson's ratio ν through

$$\kappa = \frac{E}{3\,(1-2\nu)} \quad \text{and} \quad \mu = \frac{E}{2\,(1+\nu)}. \tag{40}$$

The deviatoric part of a second order tensor with $\boldsymbol{I}$ as the identity tensor is given as $(\bullet)_{\mathrm{dev}} = \operatorname{dev}(\bullet) = (\bullet) - \frac{1}{3}\operatorname{tr}(\bullet)\boldsymbol{I}$, and positive and negative bracket operations are defined for any real number as

$$\langle\bullet\rangle_{\pm} := \frac{\bullet \pm |\bullet|}{2}\,. \tag{41}$$

The degradation function $g(d)$ is employed for representing the loss of stiffness at the macroscopic level and the change of stress responses with evolution of damage [67]. The degradation function is a monotonically decreasing function, and it satisfies the properties

$$g(d=0) = 1\,, \quad g(d=1) = 0\,, \quad \left.\frac{\partial g}{\partial d}\right|_{d=1} = 0. \tag{42}$$

The first two conditions include the limit states for unbroken and fully cracked stages. The last property also ensures that as $d \to 1$ the crack driving force attains an ultimate value [68]. In this work we employ a degradation function of the form

$$g(d) = (1-d)^2 \tag{43}$$

where a small positive value ($\approx 10^{-4}$) is added to the function to circumvent the full degradation of Ψ^{e}_{+} as well as ill posedness of equations at a fully broken stage [11,59,69]. Moreover, in this form $\frac{\partial g}{\partial d}$ at $d = 0$ is non-zero, as if that was not the case a uniform phase field of $d = 0$ would satisfy the governing equations for any state of strain and crack nucleation would never occur.

For the plastic strain energy we propose an exponential form

$$\Psi^{\mathrm{p}}(\alpha) = Q_\infty[\alpha + \frac{1}{b}(\exp(-b\alpha) - 1)]\,, \tag{44}$$

where Q_∞ and b are two material parameters defining the plastic behavior of the solid, fitted based on experimental data.

For the crack surface energy we follow the geometrical approximation introduced earlier to the form

$$\Psi^{\mathrm{f}}(d, d_{,\boldsymbol{X}}, G_c) = G_c \gamma(d, d_{,\boldsymbol{X}}). \tag{45}$$

For brittle fracture, G_c is commonly taken as a constant material parameter, independent of the loading conditions. In this work for ductile fracture, however, it is assumed that G_c degrades as a result of the stress and the inelastic strain induced in the material by the external loading. Similar ideas have been used for fatigue crack modeling [70], as well as alternative approaches for ductile fracture [31,32,55,56]. In ductile models, the degradation of G_c establishes a mechanism between plasticity and fracture, assuming that the evolution of a plastic strain measure degrades the crack resisting force through reduction of G_c, and hence, damage concentrates in regions with high values of plastic deformations. However, most phase field formulations focus only on the effects of plastic deformation, and do not consider the wide range of multi-axial stress states that a solid might experience. Accordingly, we propose a fracture toughness degradation function $\mathcal{F}$, governing the evolution of G_c in the form

$$G_c = \mathcal{F}\, G_c^0\,, \tag{46}$$

in which G_c^0 is a material constant reflecting the initial crack resistance. The exact form of $\mathcal{F}$ related to the history of a material and state of stress and strain will be determined in the next section. However, based on physical considerations we assume that

$$0 \leq \mathcal{F} \leq 1\,, \tag{47}$$

i.e., the fracture toughness G_c cannot exceed its initial value G_c^0, and it cannot take nonphysical negative values. Furthermore, considering (35) and requiring that both dissipative parts should be greater or equal to zero, we write

$$-\frac{\partial \Psi}{\partial G_c}\dot{G}_c \geq 0. \tag{48}$$

Based on the defined energy functional $\frac{\partial \Psi}{\partial G_c} = \frac{\partial \Psi^{\mathrm{f}}}{\partial G_c} = \gamma$, which is always a positive value, (48) boils down to

$$\dot{G}_c \leq 0. \tag{49}$$

This condition puts another restriction on the toughness degradation function and requires it to be non-increasing, i.e.,

$$\dot{\mathcal{F}} \leq 0. \tag{50}$$

This condition states that fracture toughness can only degrade over time (or at most stay constant) and no healing can take place. This is also in line with the physical requirement that cracks do not heal (i.e., $\dot{d} \geq 0$). It is worth mentioning that although this property arises from formulating (35) in a too restrictive manner, since in this work we are dealing with monotonic loadings, (50) is a reasonable assumption.

3.1. Plastic constitutive model

For the proposed model, a plasticity model with purely isotropic hardening, purely kinematic hardening, or a combination of the two can be used. However, since in this work we are concerned with behavior of materials under monotonic loadings, an associative isotropic elastoplastic constitutive model based on the von Mises flow theory with exponential isotropic hardening is employed. We assume isochoric plastic deformation, i.e.,

$$\det(\boldsymbol{F}^{\mathrm{p}}) = 1. \tag{51}$$

The yield function is defined as

$$\phi(\boldsymbol{\tau}, \mathcal{A}) := \|\mathrm{dev}(\boldsymbol{\tau})\| - g^{\mathrm{y}}(d)\sqrt{\tfrac{2}{3}}\Big[\tau_0 + \mathcal{A}\Big]. \tag{52}$$

Following the specific form of the elastic strain energy (39) for the Kirchhoff stress tensor (34), (52) reduces to

$$\phi(\boldsymbol{\tau}, \mathcal{A}) := g(d)\|2\mu\boldsymbol{\varepsilon}^{\mathrm{e}}_{\mathrm{dev}}\| - g^{\mathrm{y}}(d)\sqrt{\tfrac{2}{3}}\Big[\tau_0 + \mathcal{A}\Big]. \tag{53}$$

Therein, material parameter τ_0 is the initial yield stress, and $g^{\mathrm{y}}(d)$ is the yield surface degradation function with the same properties as $g(d)$ defined in (42). The degradation of the yield surface leads to an accumulation of plastic strain in damaged regions (i.e., material points with $d \geq 0$) while nonphysical elastic deformations are avoided, which is in line with experimental results as discussed in [27,32]. In addition, this yield surface degradation follows other continuum damage models that incorporate the accumulation of damage into the constitutive response such as Gurson's void growth model [51], in which the evolution of damage induces a shrinkage of the yield surface.

However, a degrading yield surface might lead to numerical difficulties. Han et al. [32] mentioned that in order to maintain computational stability for material points with value of d close to 1, the evolution of plastic deformation should be terminated, since otherwise the model may experience huge amounts of plastic deformation concentrated in severely damaged parts. As a result, to overcome this issue we propose a yield surface degradation function of the form

$$g^{\mathrm{y}}(d) = (1 - g^{\mathrm{y}}_{\infty})(1 - d)^2 + g^{\mathrm{y}}_{\infty} \tag{54}$$

with g^{y}_{∞} denoting a residual value. For small values of d, $g^{\mathrm{y}}(d) \approx g(d)$ as a result of which both the stress tensor and the plastic yield surface degrade at a similar rate. Therefore, for a yielding material point, the stress state remains on the yield surface and plastic deformation will accumulate. On the other hand, for material points characterized by large values of d, g^{y}_{∞} leads to $g^{\mathrm{y}}(d) > g(d)$ which results in a slower degradation of the plastic yield surface compared to the degradation of the stress tensor based on $g(d)$. Consequently, for severely damaged regions the stress state moves back inside the yield surface, thus limiting future plastic deformation.

Remark 1. Choosing $g^{\mathrm{y}}_{\infty} = 1$ results in $g^{\mathrm{y}}(d) = 1$, as used in [29–31], where the plastic yield surface is not degraded with the evolution of damage and material points may undergo elastic unloading. In contrast, setting $g^{\mathrm{y}}_{\infty} = 0$ results in the same function as the degrading function, i.e., $g^{\mathrm{y}}(d) = g(d)$, and thereby reduces the formulation to a plastic yield surface used in [27,71], which may cause excessive plastic deformation to concentrate in severely damaged regions. To overcome these issues, in this work a value of $g^{\mathrm{y}}_{\infty} = 0.8$ is used which gives reasonable results and helps to avoid numerical difficulties.

For describing the evolution of the plastic deformation and the internal variable, and in order to ensure a positive plastic dissipation (36), in line with the restrictive requirement on the dissipation functional (35), the principle of maximum plastic dissipation is employed. Following this principle, a Lagrange functional of the form

$$\mathcal{L} := \boldsymbol{\tau} : \left(\tfrac{1}{2}\mathcal{L}_v\boldsymbol{b}^{\mathrm{e}}\right)(\boldsymbol{b}^{\mathrm{e}})^{-1} + \mathcal{A}\dot{\alpha} + \dot{\lambda}\phi \tag{55}$$

is defined, where $\dot{\lambda}$ is a plastic Lagrange multiplier enforcing the elastic region $\phi(\boldsymbol{\tau}, \mathcal{A}) \leq 0$. The necessary conditions of this stationary principle results in the flow rule

$$\left(-\tfrac{1}{2}\mathcal{L}_v\boldsymbol{b}^{\mathrm{e}}\right)(\boldsymbol{b}^{\mathrm{e}})^{-1} = \dot{\lambda}\frac{\partial\phi}{\partial\boldsymbol{\tau}} \tag{56}$$

as well as the evolution equation of the plastic internal variable

$$\dot{\alpha} = -\dot{\lambda}\frac{\partial\phi}{\partial\mathcal{A}} \tag{57}$$

and the so-called loading–unloading conditions (Karush–Kuhn–Tucker conditions)

$$\dot{\lambda} \geq 0\,, \quad \phi \leq 0\,, \quad \dot{\lambda}\phi = 0 \tag{58}$$

for the plastic multiplier $\dot{\lambda}$. By considering plastic isotropy [72,73], zero plastic spin is assumed in the form

$$\boldsymbol{\omega}^{\mathrm{p}} = \operatorname{skew}\left(\dot{\boldsymbol{F}}^{\mathrm{p}}(\boldsymbol{F}^{\mathrm{p}})^{-1}\right) = 0 \tag{59}$$

and after simplifications, the flow rule (56) can be expressed as

$$\dot{\boldsymbol{F}}^{\mathrm{p}}(\boldsymbol{F}^{\mathrm{p}})^{-1} = \dot{\lambda}\boldsymbol{R}^{\mathrm{eT}}\frac{\partial\phi}{\partial\boldsymbol{\tau}}\boldsymbol{R}^{\mathrm{e}}\,, \tag{60}$$

where we have used the polar decomposition

$$\boldsymbol{F}^{\mathrm{e}} = \boldsymbol{R}^{\mathrm{e}}\boldsymbol{U}^{\mathrm{e}} \tag{61}$$

with $\boldsymbol{R}^{\mathrm{e}}$ as the elastic rotation tensor and $\boldsymbol{U}^{\mathrm{e}}$ as the elastic right stretch tensor.

3.2. Degradation of the fracture toughness: Stress-weighted ductile fracture model

A realistic description of ductile fracture requires a close coupling between macro and micro level phenomena, and should account for the stress state as well as plastic strain intensity. Accordingly, this section covers a micro-mechanically motivated criterion based on the history of stress and strain states for ductile crack initiation and its incorporation into the phase field model for predicting both crack initiation and advancement.

3.2.1. Fracture initiation criterion based on the stress-weighted ductile fracture model

The Stress-Weighted Ductile Fracture Model (SWDFM) [53], an uncoupled damage formulation [46,47], is incorporated into the phase field framework. Uncoupled damage models provide an estimate for the local initiation of fracture by driving the damage evolution with stress and strain states [38,39,44], where a damage field variable signals the inception of a crack when its value exceeds a critical limit. However, in these models the evolution of the damage variable is uncoupled from constitutive response of the material, and hence these models do not account for deterioration of stiffness with evolution of damage.

Similar to other uncoupled damage methods, in SWDFM a damage quantity, D_{SWDFM}, is calculated based on histories of plastic strain and stress, and its rate form is given as

$$\dot{D}_{\mathrm{SWDFM}} = f(I_1, J_2, J_3, \dot{\alpha}). \tag{62}$$

In this equation $I_1 = \operatorname{tr}(\boldsymbol{\tau})$ is the first invariant of the Kirchhoff stress tensor, $J_2 = \frac{1}{2}\operatorname{tr}\left(\boldsymbol{\tau}_{\mathrm{dev}}^2\right)$ is the second invariant of the deviatoric part of the Kirchhoff stress tensor, $J_3 = \det\left(\boldsymbol{\tau}_{\mathrm{dev}}\right)$ is the third invariant of the deviatoric part of the Kirchhoff stress tensor, and $\dot{\alpha}$ is the rate of the plastic internal variable. For SWDFM, this dependency on the invariants is expressed using the stress triaxiality and the Lode angle parameter. The stress triaxiality T is defined as

$$T := \frac{\tau_m}{\sqrt{3J_2}}\,, \tag{63}$$

with $\tau_m = \frac{1}{3}I_1$ as the hydrostatic Kirchhoff stress. The Lode angle parameter ζ is related to the Lode angle θ, and is defined as

$$\zeta := \cos(3\theta) = \frac{3\sqrt{3}J_3}{2(J_2)^{3/2}}. \tag{64}$$

The Lode angle parameter is in the range $-1 \leq \zeta \leq 1$, and it distinguishes between the type of stress states, e.g., axisymmetric tensile ($\zeta = 1$), axisymmetric compressive ($\zeta = -1$), or pure shear ($\zeta = 0$) states.

With these quantities, similar to the analytical formulation of Rice and Tracey [39], and following the work of Smith et al. [52], specific form of the SWDFM is written as

$$f(T, \zeta, \dot{\alpha}) = \mathcal{C}\left(\left[\exp(1.3T) - \frac{1}{\mathcal{B}}\exp(-1.3T)\right]\exp(\mathcal{K}(|\zeta| - 1))\right)\dot{\alpha}. \tag{65}$$

Parameters $\mathcal{C}$, $\mathcal{B}$, and $\mathcal{K}$ are material constants, which are calibrated based on experimental tests [54]. Parameter $\mathcal{C}$ is inversely related to deformation capacity of the body, where a higher value causes the damage to grow faster. The term involving $\mathcal{B}$, distinguishes between void growth and shrinkage rates, where $\mathcal{B} > 1$ biases the damage rate towards positive levels of stress triaxiality. This parameter is also used to model the response of the material under cyclic loadings [53]. The parameter $\mathcal{K}$ reflects the influence of the Lode angle parameter and can take positive or negative values.

Finally, using (65) the damage quantity is defined in the form

$$D_{\mathrm{SWDFM}} = \mathcal{C} \int_0^{\alpha} \left(\left[\exp(1.3T) - \frac{1}{\mathcal{B}} \exp(-1.3T) \right] \exp(\mathcal{K}(|\zeta| - 1)) \right) \mathrm{d}\alpha \leq 1 \tag{66}$$

which indicates the initiation of a crack as soon as $D_{\mathrm{SWDFM}} = 1$.

3.2.2. Combination of the stress-weighted ductile fracture and phase field models

For the proposed framework, G_c is assumed to be a non-constant property, depending on the loading conditions and the stress–strain history of the material. Similar concepts have been used in the literature [31,32,55,56]; however, they mostly concentrate on the effects of plastic deformations, and do not account for stress triaxiality and the Lode angle parameter. To account for the latter, we incorporate the SWDFM approach in (46) for degrading the fracture resistance, and propose a fracture degradation function of the form

$$\mathcal{F} := (1 - \mathcal{F}_{\infty})(1 - D_{\mathrm{SWDFM}})^2 + \mathcal{F}_{\infty} \tag{67}$$

where similar to the degradation function, a residual positive value $\mathcal{F}_{\infty}$ ($\approx 10^{-1}$) is used to avoid numerical difficulties arising from full degradation of the fracture toughness.

This approach has several advantages: (i) through degradation of fracture toughness damage concentrates in regions with high values of D_{SWDFM} a quantity that takes into account plastic deformation, stress triaxiality and the Lode angle parameter. As a result, evolution of damage is coupled with evolution of stress–strain states; (ii) the use of the SWDFM in context of the phase field formulation allows the transformation of the uncoupled SWDFM criterion to a more realistic coupled formulation where evolution of damage affects the constitutive response of the material through degradation of stiffness and shrinkage of the plastic yield surface; (iii) this proposition allows the use of the SWDFM originally developed as a criterion for ductile crack initiation, as a method for predicting crack inception and propagation.

Due to the integration of the SWDFM and the phase field model into a coupled framework, the material parameters $\mathcal{C}$, $\mathcal{B}$, and $\mathcal{K}$ are in general different from those reported for the uncoupled SWDFM in [54,74,75]. However, for the calibration process, a similar procedure as discussed in [54] can be used. Accordingly, first a loading condition with $\zeta = 1$ is studied using an axisymmetric specimen loaded in monotonic tension. Given high level of stress triaxiality, even for $\mathcal{B} \neq 1$, $\left(\exp(1.3T) - \frac{1}{\mathcal{B}}\exp(-1.3T)\right) \approx \exp(1.3T)$. Consequently parameter $\mathcal{C}$ can be adjusted independently based on the point of fracture identified by the sudden drop in the measured load–displacement curve. Under cyclic loadings, parameter $\mathcal{B}$ can be identified, and a third test with an intermediate value of the Lode angle parameter may be used to calibrate $\mathcal{K}$. However, since in this work we are concerned with monotonic loadings, in line with [53], a value of $\mathcal{B} = 2$ is used throughout this work. Furthermore, as shown in Section 5 we use a value of $\mathcal{K} = 0.5$ for all the examples, which is again in line with the value reported in [53] based on experimental tests. As a result, two out of the three parameters required for the SWDFM are assumed fixed in this work, which as discussed in [53], renders the proposed model to be significantly easier to calibrate and apply.

Remark 2. In the present work, the value of G_c^0 is chosen such that the numerical results match the test data in capturing the experimental peak load. The first reason for this is that the geometrical approximation of the crack surface (9) alongside the length scale parameter l, cause the crack resistance parameter G_c^0 to be different from the so called Griffith energy release rate determined commonly from experiments. Secondly, introduction of the SWDFM into the evolution of G_c couples the phase field parameters to those of the SWDFM, which might require a set of specific experiments to determine the parameters. As a result, further investigation is needed to relate the G_c^0 parameter to a material parameter found by experimental tests.

3.3. Restrictions on the fracture toughness degradation function

Following the second law of thermodynamics and for the first time, to the best of our knowledge, we impose an exact requirement on the degradation of fracture toughness. Following (35) the reduced dissipation function is expressed as

$$\boldsymbol{\tau} : \left(-\tfrac{1}{2}\mathcal{L}_v \boldsymbol{b}^{\mathrm{e}}\right)(\boldsymbol{b}^{\mathrm{e}})^{-1} - \mathcal{A}\dot{\alpha} \geq \gamma \dot{\mathcal{F}} G_c^0. \tag{68}$$

Using the flow rule (56) and the evolution equation for the internal plastic variable (57), this inequality is reformed into

$$\dot{\lambda}\left(\boldsymbol{\tau} : \frac{\partial \phi}{\partial \boldsymbol{\tau}} + \mathcal{A}\frac{\partial \phi}{\partial \mathcal{A}}\right) \geq \gamma \dot{\mathcal{F}} G_c^0. \tag{69}$$

Following the specific form of the yield function given in (52), this turns into

$$\dot{\lambda}\left(\boldsymbol{\tau} : \frac{\operatorname{dev}(\boldsymbol{\tau})}{\|\operatorname{dev}(\boldsymbol{\tau})\|} - g^{\mathrm{y}}(d)\sqrt{\tfrac{2}{3}}\mathcal{A}\right) \geq \gamma \dot{\mathcal{F}} G_c^0. \tag{70}$$

By adding and subtracting $g^{\mathrm{y}}(d)\sqrt{\frac{2}{3}}\tau_0$ and using the fact that $\boldsymbol{\tau} : \frac{\operatorname{dev}(\boldsymbol{\tau})}{\|\operatorname{dev}(\boldsymbol{\tau})\|} = \|\operatorname{dev}(\boldsymbol{\tau})\|$, the inequality is stated as

$$\dot{\lambda}\phi + \dot{\lambda} g^{\mathrm{y}}(d)\sqrt{\tfrac{2}{3}}\tau_0 \geq \gamma \dot{\mathcal{F}} G_c^0. \tag{71}$$

However, based on the KKT conditions $\dot{\lambda}\phi = 0$, the relation simplifies into

$$\dot{\lambda} g^{\mathrm{y}}(d)\sqrt{\tfrac{2}{3}}\frac{\tau_0}{G_c^0} \geq \gamma \dot{\mathcal{F}}. \tag{72}$$

Finally (assuming $\gamma \neq 0$) the rate of fracture toughness degradation function should satisfy the inequality

$$\dot{\mathcal{F}} \leq \frac{\dot{\lambda} g^{\mathrm{y}}(d)}{\gamma}\left(\sqrt{\tfrac{2}{3}}\frac{\tau_0}{G_c^0}\right). \tag{73}$$

As apparent from this equation, requirement (50) is a special case of this more general condition. Constraint (73) is the thermodynamic requirement, however, since in this work we are dealing with monotonic loading and do not consider crack healing, the stricter condition (50) is enforced. On the other hand, accounting for crack healing under special circumstances such as cyclic loading might be formulated based on the less restricting equation (73).

4. Governing equations and finite element implementation

4.1. Strong form of the governing equations

Inserting the results of (33) into (16), and assuming quasi-static loading without body forces $\boldsymbol{B} = \mathbf{0}$, we obtain the strong form of the equilibrium equation

$$\operatorname{div}(\boldsymbol{\sigma}) = 0 \quad \text{in } V \tag{74}$$

with the Cauchy stress $\boldsymbol{\sigma} = \frac{1}{J}\boldsymbol{\tau}$ and the Kirchhoff stress $\boldsymbol{\tau}$ defined in (34).

From (19), and assuming $h = 0$, the strong form of the crack phase field equation is obtained as

$$\operatorname{Div}\left(\frac{\partial \Psi^{\mathrm{f}}}{\partial d_{,\boldsymbol{X}}}\right) = \frac{\partial g}{\partial d}\Psi_+^{\mathrm{e}} + \frac{\partial \Psi^{\mathrm{f}}}{\partial d} \quad \text{in } V_0 \tag{75}$$

which by using the specific form of fracture energy in (45), becomes

$$\operatorname{Div}(G_c\, l\, d_{,\boldsymbol{X}}) = \frac{\partial g}{\partial d}\Psi_+^{\mathrm{e}} + \frac{G_c}{l} d \quad \text{in } V_0. \tag{76}$$

4.2. Requirements for crack irreversibility

To enforce an irreversibility of crack growth for brittle fracture, Miehe et al. [11] introduced a history functional of the form

$$\mathcal{H}(\boldsymbol{\varepsilon}^{\mathrm{e}}, t) := \max_{\hat{t} \leq t} \Psi_{+}^{\mathrm{e}}(\boldsymbol{\varepsilon}^{\mathrm{e}}, \hat{t}) \tag{77}$$

which replaces Ψ_{+}^{e} in the governing equation. This idea was extended by Yin and Kaliske [31] to ductile fracture, expressing the governing equation as

$$\mathrm{Div}(G_c\, l\, d_{,\boldsymbol{X}}) = \frac{\partial g}{\partial d}\mathcal{H} + \frac{G_c}{l}d \quad \text{in } V_0 \tag{78}$$

where in contrast to [11], G_c is assumed to be a changing variable, which can stay constant or decrease depending on the evolution of a plastic measure. However, for the most general case of an increasing or decreasing fracture toughness G_c, the use of a history functional might violate the inequality $\dot{d} \geq 0$, as (77) is not a sufficient condition to satisfy the crack irreversibility. To illustrate this issue, we consider an example and without loss of generality assume $d_{,\boldsymbol{X}} = \mathbf{0}$, leading to the phase field equation (78) over V_0 of the form

$$2(1-d)\mathcal{H} = \frac{\mathcal{F}\, G_c^0}{l}d \tag{79}$$

where we have used (43) and (46). After straightforward calculations, the evolution of the phase field parameter is given as

$$\dot{d} = \frac{2\, l\, G_c^0 \left(\dot{\mathcal{H}}\mathcal{F} - \mathcal{H}\dot{\mathcal{F}}\right)}{\left(2\, l\, \mathcal{H} + \mathcal{F}\, G_c^0\right)^2}. \tag{80}$$

Accordingly, the crack irreversibility requirement reduces into

$$\dot{\mathcal{H}}\mathcal{F} - \mathcal{H}\dot{\mathcal{F}} \geq 0. \tag{81}$$

Due to its nature $\dot{\mathcal{H}} \geq 0$, and if we enforce the strong requirement (50) on $\dot{\mathcal{F}}$, (81) is satisfied a priori. However, if we use the exact requirement (73) for $\dot{\mathcal{F}}$, (81) might not be satisfied in general. As a result, we conclude that for the most general case use of the history variable approach with an evolving fracture toughness does not guarantee the crack irreversibility. Hence, to circumvent such a violation, in the present work the crack irreversibility requirement is satisfied node-wise with a primal–dual active set strategy [76].

4.3. Weak form of the governing equations

Using the method of weighted residuals and by multiplying (74) with the test function of the displacement field $\delta\boldsymbol{u}$, we obtain

$$\int_V \mathrm{div}(\boldsymbol{\sigma}) \cdot \delta\boldsymbol{u}\, \mathrm{d}V = 0. \tag{82}$$

After simplifications this leads to

$$\int_{A_t} \boldsymbol{\sigma}\boldsymbol{n} \cdot \delta\boldsymbol{u}\, \mathrm{d}A - \int_V \boldsymbol{\sigma} : \delta\boldsymbol{u}_{,\boldsymbol{x}}\, \mathrm{d}V = 0\,, \tag{83}$$

with $\boldsymbol{n}$ as the outward unit vector normal to A_t, the surface in the deformed configuration over which the Neumann-type boundary conditions are defined.

Similarly we can find the weak form of the crack equation as

$$\int_{V_0} \left(\mathrm{Div}(G_c l d_{,\boldsymbol{X}}) - \frac{\partial g}{\partial d}\Psi_{+}^{\mathrm{e}} - \frac{G_c}{l}d\right)\delta d\, \mathrm{d}V_0 = 0\,, \tag{84}$$

where δd is the test field for the phase field. After some simplifications we obtain

$$\int_{V_0} \left(\mathcal{F}\, G_c^0\, l\, d_{,\boldsymbol{X}} \cdot \delta d_{,\boldsymbol{X}} + \frac{\partial g}{\partial d}\Psi_{+}^{\mathrm{e}}\delta d + \frac{\mathcal{F}G_c^0}{l}d\delta d\right) \mathrm{d}V_0 = 0\,, \tag{85}$$

where we have used the fact that

$$d_{,X} \cdot N = 0 \quad \text{on} \quad A_0. \tag{86}$$

This boundary condition is imposed to enforce the crack evolution by mechanical loads only and no other external sources, indicating that crack phase field is passive in nature and external driving via boundary conditions is not allowed [10,77–79]. Furthermore, in (85) the gradient of the crack phase field, the term responsible for diffusing the crack surface, is multiplied by the toughness degradation function $\mathcal{F}$. Accordingly, if $\mathcal{F} \to 0$, the gradient term vanishes, which in turn would make the formulation mesh sensitive. As a result, as shown in (67), a residual value $\mathcal{F}_\infty$ is required to obtain a mesh objective formulation.

4.4. Finite element implementation

The spatial discretization of the weak from is performed by means of the Galerkin method. We discretize the displacement field within an element as

$$u_i = \sum_{A=1}^{\mathrm{N_{node}}} N^A \bar{u}_i^A \,, \tag{87}$$

where N^A is the shape function used for the displacement field at node A, and $\bar{u}_i^A$ is the i^{th} component of the nodal value of the displacement vector at node A. Similarly, in a Bubnov Galerkin context, we choose an approximation for the test displacement field as

$$\delta u_i = \sum_{A=1}^{\mathrm{N_{node}}} N^A \delta \bar{u}_i^A \tag{88}$$

and its derivative with respect to x_j is approximated as

$$\delta u_{i,j} = \sum_{A=1}^{\mathrm{N_{node}}} N^A_{,j} \delta \bar{u}_i^A. \tag{89}$$

Using the discretized fields, the residual form of the mechanical problem at node A and direction i reads as

$$(\mathcal{R}_u)_i^A = \sum_{j=1}^{\mathrm{nd}} \left(\int_{A_t} \sigma_{ij} n_j N^A \,\mathrm{d}A - \int_V \sigma_{ij} N^A_{,j} \,\mathrm{d}V \right). \tag{90}$$

Next, we discretize the crack phase field within an element using discrete nodal values with a form

$$d = \sum_{A=1}^{\mathrm{N_{node}}} N^A \bar{d}^A \tag{91}$$

where N^A is the shape function at node A, and $\bar{d}^A$ is the corresponding value of the phase field parameter at that node. Furthermore, for the derivative of this field with respect to X_I we can write

$$d_{,I} = \sum_{A=1}^{\mathrm{N_{node}}} N^A_{,I} \bar{d}^A. \tag{92}$$

Using the same shape functions for the test fields leads to

$$\delta d = \sum_{A=1}^{\mathrm{N_{node}}} N^A \delta \bar{d}^A \qquad \text{and} \qquad \delta d_{,I} = \sum_{A=1}^{\mathrm{N_{node}}} N^A_{,I} \delta \bar{d}^A. \tag{93}$$

As a result, the residual form of the crack problem at node A is obtained as

$$(\mathcal{R}_d)^A = \int_{V_0} \Big(\sum_{I=1}^{\mathrm{nd}} \mathcal{F}\, G_c^0\, l d_{,I} N^A_{,I} + \frac{\partial g}{\partial d} \Psi_+^{\mathrm{e}} N^A + \frac{\mathcal{F} G_c^0}{l} d N^A \Big) \,\mathrm{d}V_0. \tag{94}$$

4.5. Finite strain plasticity return mapping algorithm

The numerical integration of the constitutive relations is done using the so-called elastic predictor/plastic corrector algorithm, commonly also called the "Stress Return Algorithm (Return Mapping)". Following this procedure outlined in, e.g., [66], we assume that for each time interval $[t_n, t_{n+1}]$, the initial state defined by $\boldsymbol{\varepsilon}^{\mathrm{e}}_n$, α_n, and $\boldsymbol{F}_n$ is known. The configuration at time t_{n+1} is obtained from the incremental displacement field, and leads to the current deformation gradient $\boldsymbol{F}_{n+1}$. The incremental deformation gradient $\boldsymbol{F}_{\Delta}$ is defined as

$$\boldsymbol{F}_{\Delta} := \boldsymbol{F}_{n+1}\boldsymbol{F}_n^{-1}. \tag{95}$$

Next, for determining whether the load increment is elastic or elastoplastic, we assume an elastic trial state with $\alpha^{\mathrm{trial}}_{n+1} = \alpha_n$ and

$$\boldsymbol{b}^{\mathrm{e\,trial}}_{n+1} = \boldsymbol{F}_{\Delta}\boldsymbol{b}^{\mathrm{e}}_n\boldsymbol{F}^{\mathrm{T}}_{\Delta}\,, \tag{96}$$

computing the value of $\boldsymbol{b}^{\mathrm{e}}_n$ from the known value of $\boldsymbol{\varepsilon}^{\mathrm{e}}_n$. With the trial value of the left Cauchy–Green strain tensor at hand, the trial elastic Eulerian logarithmic strain tensor is computed as

$$\boldsymbol{\varepsilon}^{\mathrm{e\,trial}}_{n+1} = \tfrac{1}{2}\ln\left(\boldsymbol{b}^{\mathrm{e\,trial}}_{n+1}\right). \tag{97}$$

The trial value of the Kirchhoff stress tensor (34) considering the specific form of the elastic strain energy (39) is calculated as

$$\boldsymbol{\tau}^{\mathrm{trial}}_{n+1} = g(d)\left(\kappa\langle\mathrm{tr}\,\boldsymbol{\varepsilon}^{\mathrm{e\,trial}}_{n+1}\rangle_{+}\boldsymbol{I} + 2\mu(\boldsymbol{\varepsilon}^{\mathrm{e\,trial}}_{n+1})_{\mathrm{dev}}\right) + \kappa\langle\mathrm{tr}\,\boldsymbol{\varepsilon}^{\mathrm{e\,trial}}_{n+1}\rangle_{-}\boldsymbol{I}\,. \tag{98}$$

Using the trial values, the yield function is evaluated as

$$\phi^{\mathrm{trial}}_{n+1} = \|\mathrm{dev}(\boldsymbol{\tau}^{\mathrm{trial}}_{n+1})\| - g^{\mathrm{y}}(d)\sqrt{\tfrac{2}{3}}\left[\tau_0 + \mathcal{A}^{\mathrm{trial}}_{n+1}\right] \tag{99}$$

with

$$\mathcal{A}^{\mathrm{trial}}_{n+1} = Q_{\infty}[1 - \exp(-b\alpha^{\mathrm{trial}}_{n+1})]. \tag{100}$$

If $\phi^{\mathrm{trial}}_{n+1} \leq 0$ the load increment is purely elastic, and the elastic trial is accepted as the updated configuration. Otherwise, if $\phi^{\mathrm{trial}}_{n+1} > 0$, the trial state is not admissible, i.e., the load increment is elastoplastic and a plastic corrector is computed. Therefore, the plastic strain increment as well as updated values of $\boldsymbol{\tau}_{n+1}$ and $\mathcal{A}_{n+1}$ are computed, such that the stress state is projected back on the yield surface. Those increments are determined by discretization of the evolution equations for the plastic flow rule (60) and the internal variable (57). A backward Euler discretization of the evolution equation (57) leads to

$$\alpha_{n+1} = \alpha_n + \sqrt{\tfrac{2}{3}}\Delta\lambda. \tag{101}$$

Using a backward exponential integrator for (60) leads to

$$\boldsymbol{F}^{\mathrm{p}}_{n+1} = \boldsymbol{R}^{\mathrm{e\,T}}_{n+1}\exp\left(\Delta\lambda\left.\frac{\partial\phi}{\partial\boldsymbol{\tau}}\right|_{n+1}\right)\boldsymbol{R}^{\mathrm{e}}_{n+1}\boldsymbol{F}^{\mathrm{p}}_n\,, \tag{102}$$

where the isochoric nature of the plastic deformation, i.e., $\det(\boldsymbol{F}^{\mathrm{p}}) = 1$, for pressure insensitive flow potentials is carried over exactly for a traceless flow vector, $\frac{\partial\phi}{\partial\boldsymbol{\tau}}$. A substantial simplification of the return–mapping algorithm can be achieved by rewriting this equation equivalently in terms of the logarithmic elastic strain measure as

$$\boldsymbol{\varepsilon}^{\mathrm{e}}_{n+1} = \boldsymbol{\varepsilon}^{\mathrm{e\,trial}}_{n+1} - \Delta\lambda\left.\frac{\partial\phi}{\partial\boldsymbol{\tau}}\right|_{n+1} \tag{103}$$

which for the yield function in this work simplifies into

$$\boldsymbol{\varepsilon}^{\mathrm{e}}_{n+1} = \boldsymbol{\varepsilon}^{\mathrm{e\,trial}}_{n+1} - \Delta\lambda\mathcal{N}_{n+1} \tag{104}$$

with

$$\mathcal{N}_{n+1} = \frac{\mathrm{dev}(\boldsymbol{\tau}_{n+1})}{\|\mathrm{dev}(\boldsymbol{\tau}_{n+1})\|}. \tag{105}$$

As it is evident from the equations, use of the elastic logarithmic strain has led to a simple evolution equation that resembles its small strain counterpart. With these values we can find the updated forces as

$$\mathcal{A}_{n+1} = Q_\infty \left[1 - \exp\left(-b\left(\alpha_n + \sqrt{\tfrac{2}{3}}\Delta\lambda\right)\right)\right] \tag{106}$$

and

$$\boldsymbol{\tau}_{n+1} = \boldsymbol{\tau}^{\text{trial}}_{n+1} - 2g(d)\,\mu\,\Delta\lambda\,\mathcal{N}^{\text{trial}}_{n+1} \tag{107}$$

where we have used the fact that

$$\mathcal{N}_{n+1} = \mathcal{N}^{\text{trial}}_{n+1} = \frac{\operatorname{dev}(\boldsymbol{\tau}^{\text{trial}}_{n+1})}{\|\boldsymbol{\tau}^{\text{trial}}_{n+1}\|}. \tag{108}$$

Finally we can form the consistency condition and write

$$\phi_{n+1} = \|\operatorname{dev}(\boldsymbol{\tau}_{n+1})\| - g^{\text{y}}(d)\sqrt{\tfrac{2}{3}}\left[\tau_0 + \mathcal{A}_{n+1}\right] = 0. \tag{109}$$

This equation can be solved for the value of incremental plastic multiplier $\Delta\lambda$ which is then used in (101) and (104) to update the state and bring it back to the yield surface.

5. Numerical results

The proposed phase field model is validated by means of a numerical study of experimental tests, considering different levels of stress triaxiality and the Lode angle parameter. Fig. 3 schematically depicts the resulting levels of stress triaxiality T, and values of the Lode angle parameter ζ at the respective location of crack initiation for different, commonly employed experimental tests.

In this work, for assessing the proposed model considering different values of T and ζ, we investigate

- two different geometries of the Cylindrical Notched Tension (CNT) test performed by Kanvinde and Deierlein [74], characterized by a moderate to high stress triaxiality and an axisymmetric stress state with the Lode angle parameter of $\zeta = 1$ at the center of specimen where the crack initiates,
- the Grooved Plate (GP) test done by Terashima and Deierlein [75], characterized by a high stress triaxiality with $\zeta = 0$ at the location of crack initiation, i.e., midpoint of the notched region,
- the Blunt Notch (BN) test investigated by Ziccarelli [54], for a combination of low to moderate stress triaxiality, and an intermediate Lode angle parameter in the range of $0 < \zeta < 1$ at the location of crack initiation.

The subsequently presented numerical results are obtained using RACCOON [80,81], see also [56,82], a massively parallel finite element library developed upon MOOSE [83]. For the time stepping procedure within the incremental-iterative nonlinear solution algorithm, we follow a staggered scheme similar to [11,84], where at each loading step the equilibrium equation (90) and the phase field equation (94) are decoupled and solved alternately. In this scheme at each loading step, while the phase field is held constant, initially the equilibrium equation is solved for the displacement field with the help of the Newton–Raphson method. Next the displacement field is held constant and the crack evolution equation is solved using PETSc's variational inequality solver [76]. The simulation advances to the next loading step when the residual of the equilibrium equation is less than a prescribed threshold. We also mention that another technique for solving the governing equations is the monolithic scheme, in which equations are solved for all the unknowns simultaneously. However, due to robustness issues encountered in our numerical simulations, also documented in [26], we utilize the staggered scheme in this work.

For identifying the material parameters for each test, the elastoplastic parameters, i.e., constants E, ν, τ_0, Q_∞, and b, are calibrated first such that the behavior of the solid before cracking (pre-peak behavior) is captured. For calibrating the rest of the parameters, i.e., G_c^0, $\mathcal{C}$, $\mathcal{B}$, and $\mathcal{K}$, the fracture response of the material is considered. For these parameters, the method outlined in Section 3.2.2 is utilized.

5.1. Cylindrical notched tension (CNT) test

The first considered example is the Cylindrical Notched Tension (CNT) test. CNT tests, as a result of the specimen geometry, are widely used to investigate ductile fracture under axisymmetric stress states with Lode

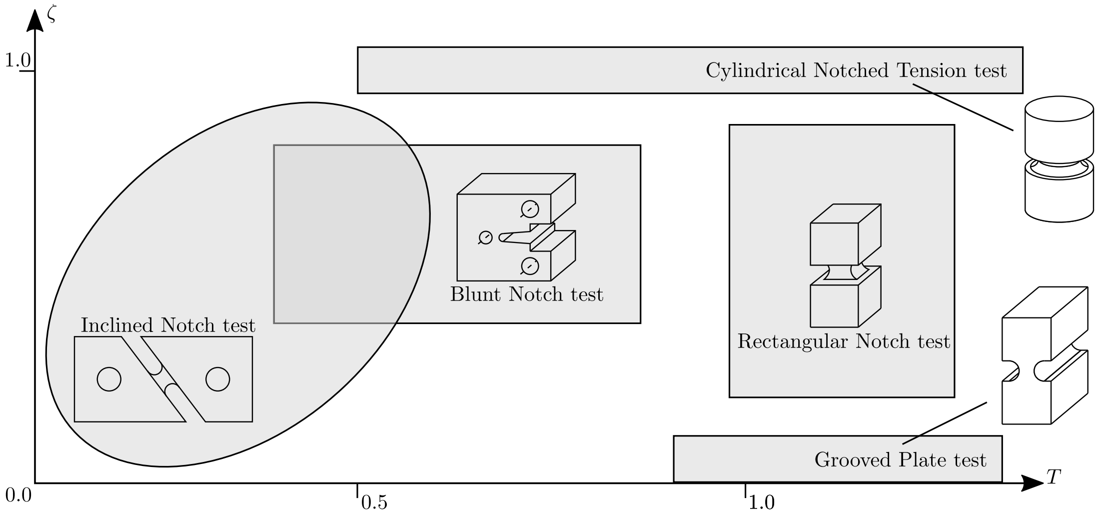

Fig. 3. Level of stress triaxiality and Lode angle parameter at fracture locus for various common experimental tests. *Source:* Adopted from [53].

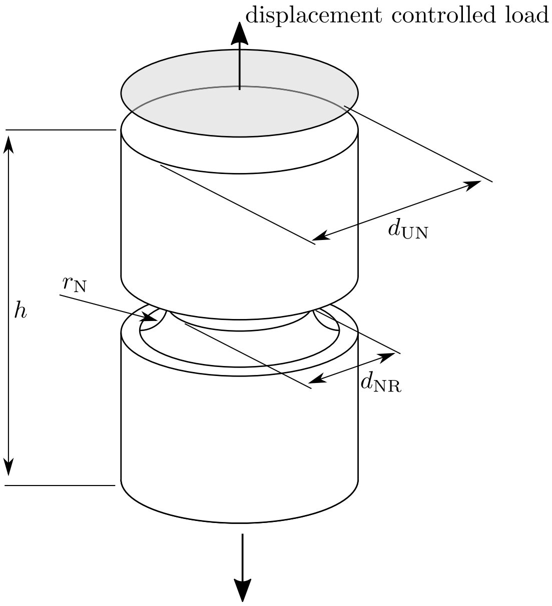

Fig. 4. Geometry of the CNT specimen. For the loading, the top and bottom surfaces of the specimen are pulled vertically in a displacement controlled manner.

angle parameters close to unity, i.e., $\zeta \approx 1$, and moderate to high values of stress triaxiality at the location of crack initiation. The test setup of the CNT test alongside the loading conditions are illustrated in Fig. 4. As discussed in [53,85], an increase in the ratio $d_{\mathrm{UN}}/r_{\mathrm{N}}$ leads to higher values of the stress triaxiality at the center of the specimen where the crack initiates. Accordingly, to capture different level of stress triaxiality, we consider two different geometries, characterized by $r_{\mathrm{N}} = 1.59$ mm and $r_{\mathrm{N}} = 3.18$ mm. The employed geometrical dimensions for the two cases are summarized in Table 1.

In the finite element model, axisymmetry and vertical symmetry are exploited. For both geometries, quadrilateral elements with a characteristic element size of 0.04 mm in areas where the crack is expected to propagate are used. In line with the suggestions made in [10,61,86] that the length scale parameter should be at least twice the size

Table 1
Dimensions for the CNT specimens with small and large notch radii.

d_{UN} (mm)	d_{NR} (mm)	r_{N} (mm)	h (mm)
12.7	6.35	1.59	25.4

d_{UN} (mm)	d_{NR} (mm)	r_{N} (mm)	h (mm)
12.7	6.35	3.18	25.4

Table 2
Parameters for the CNT tests.

A572 Grade 50 steel								
E (GPa)	ν (–)	τ_0 (MPa)	Q_∞ (MPa)	b (–)	G_c^0 (N/mm)	$\mathcal{C}$ (–)	$\mathcal{B}$ (–)	$\mathcal{K}$ (–)
205	0.3	345	380	18	95	0.9	2	0.5
A709 Grade 70 steel								
E (GPa)	ν (-)	τ_0 (MPa)	Q_∞ (MPa)	b (–)	G_c^0 (N/mm)	$\mathcal{C}$ (–)	$\mathcal{B}$ (–)	$\mathcal{K}$ (–)
205	0.3	551	310	14	100	0.28	2	0.5

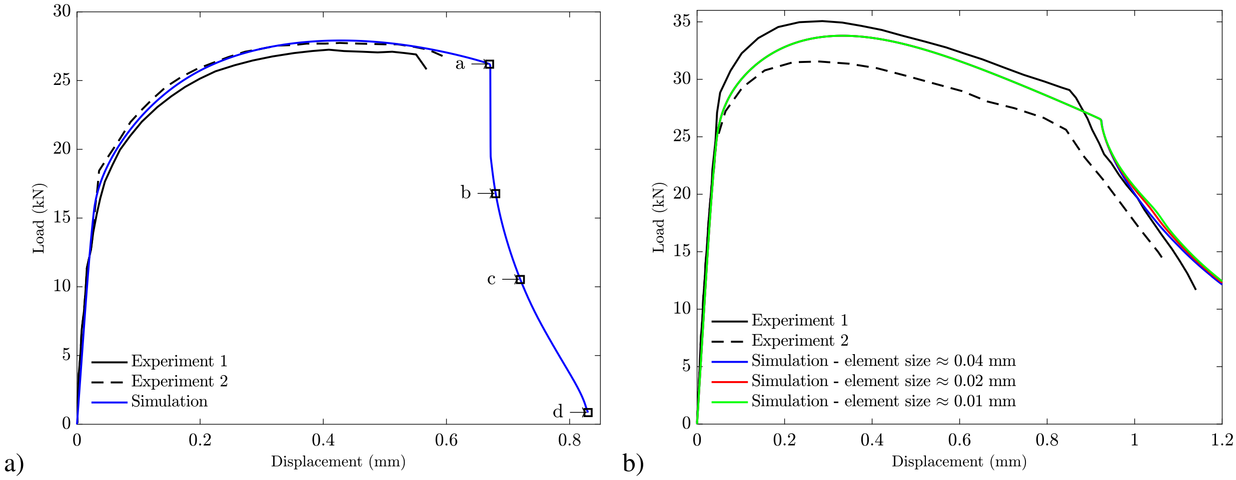

Fig. 5. Computed and experimental (conducted by Kanvinde and Deierlein [74]) load–displacement curves for the CNT specimen with $r_{\text{N}} = 1.59$ mm for (a) the A572 Grade 50 steel and (b) the A709 Grade 70 steel. Markers shown on the load–displacement curve correspond to the evaluation plots shown in Fig. 9.

of elements, a length scale of $l = 0.25$ mm is used. Furthermore, to demonstrate the suitability of the model for different materials, two different grades of structural steel, namely the A572 Grade 50 steel and the A709 Grade 70 steel, are investigated. The employed material properties for the two different materials were calibrated based on experimental results and they are summarized in Table 2.

The obtained load–displacement curves for the geometries with $r_{\text{N}} = 1.59$ mm and $r_{\text{N}} = 3.18$ mm alongside the experimental data for both materials are presented in Figs. 5 and 6, respectively. A good agreement between the simulated results and the experiments is obtained. The proposed framework accurately captures the fracture initiation and propagation by using a set of parameters that only depend on the used material and not the geometry of the specimen or the stress state at the crack initiation location. Furthermore, Fig. 5b demonstrates the mesh objectivity of the proposed framework for three levels of finite element refinements with element sizes of 0.04 mm, 0.02, and 0.01 mm.

The evolution of the crack phase field d and the internal plastic variable α at the location of crack initiation, i.e., the center of the specimen, for selected CNT tests are shown in Fig. 7. The introduction of the yield surface degradation function $g^{\text{y}}(d)$ in (54) leads to an accumulation of plastic strain at damaged material points, which is in line with experimental observations [27,32]. Furthermore, parameter g_∞^{y} prevents the accumulation of plastic deformation for severely damaged material points, which in turn maintains the computational stability of the simulations.

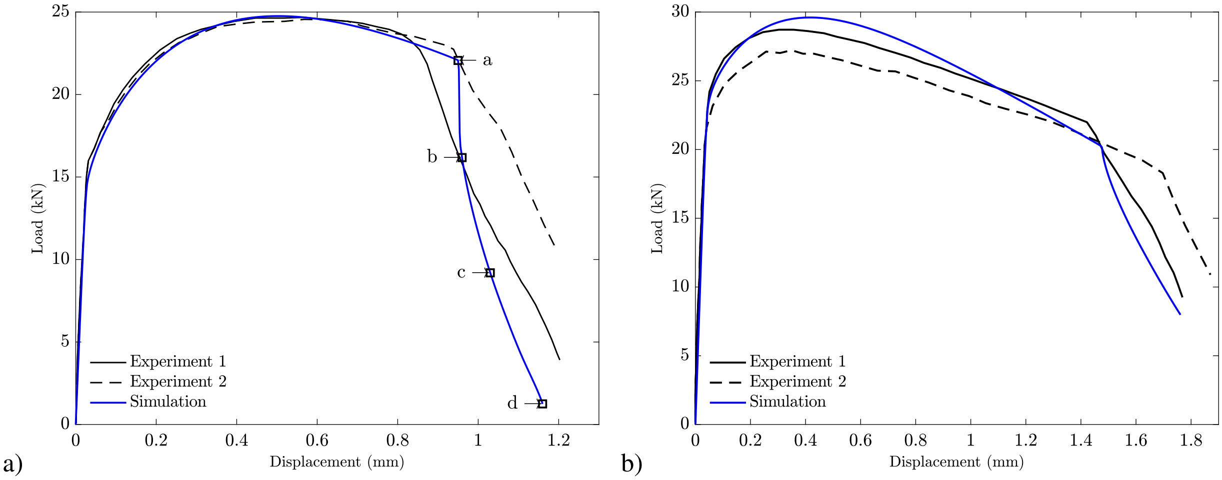

Fig. 6. Computed and experimental (conducted by Kanvinde and Deierlein [74]) load–displacement curves for the CNT tests with r_N = 3.18 mm for (a) the A572 Grade 50 steel and (b) the A709 Grade 70 steel. Markers shown on the load–displacement curve correspond to the evaluation plots shown in Fig. 10.

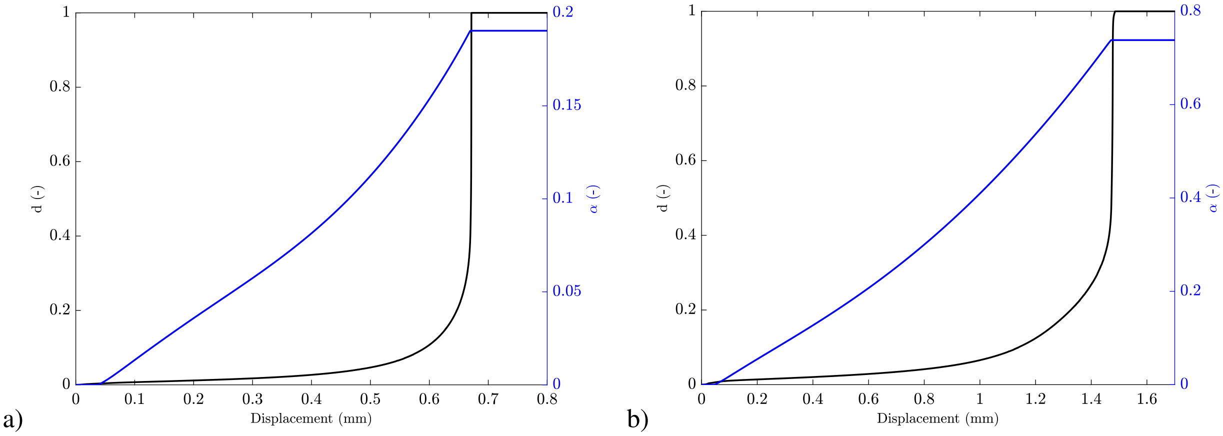

Fig. 7. Evolution of the crack phase field d and the internal plastic strain variable α at the location of crack initiation for (a) the $r_N = 1.59$ mm specimen with the A572 Grade 50 steel and (b) the $r_N = 3.18$ mm specimen with the A709 Grade 70 steel.

Figs. 8a and 8b depict the radial distribution of the stress triaxiality and the Lode angle parameter along the plane of vertical symmetry of the specimen for the A572 Grade 50 steel once the phase field parameter attains a value of $d = 0.05$ and a macroscopic crack starts to form. This figure illustrates the axisymmetric stress state of the CNT tests with $\zeta \approx 1$, as well as the influence of the value of r_N in producing moderate to high levels of stress triaxiality at the center of the specimens. Similarly, Figs. 8c and 8d depict the radial distribution of the internal plastic variable and the SWDFM damage quantity. Unlike the stress triaxiality, the internal plastic variable attains its maximum value at the outer surface of the specimen. The SWDFM accounts for the combined effects of the plastic deformation and the stress state, and leads to an accurate prediction of the crack initiation at the center of the specimen, which is in line with experimental observations. Figs. 9 and 10 show selected stages of the evolution of the crack phase field until complete failure for the A572 Grade 50 steel for both geometries. In both cases, the crack initiates at the center of the specimen, where triaxiality attains its maximum, and it propagates in the radial direction until final rupture.

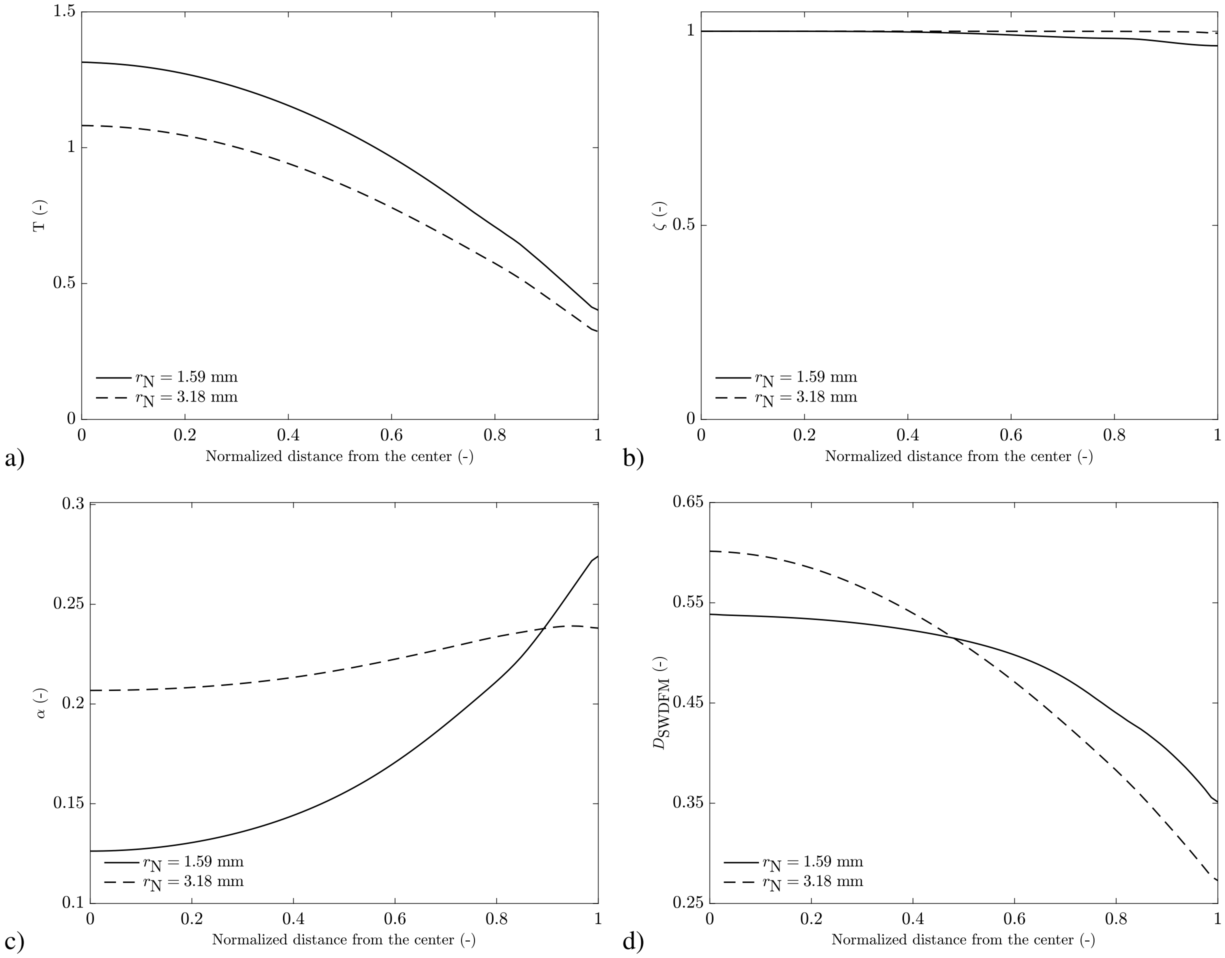

Fig. 8. Radial distribution of (a) the stress triaxiality T, (b) the Lode angle parameter ζ, (c) the internal plastic variable α, and (d) the SWDFM damage quantity D_{SWDFM} over the center line of the CNT specimens for the A572 Grade 50 steel once $d = 0.05$ at the crack initiation location.

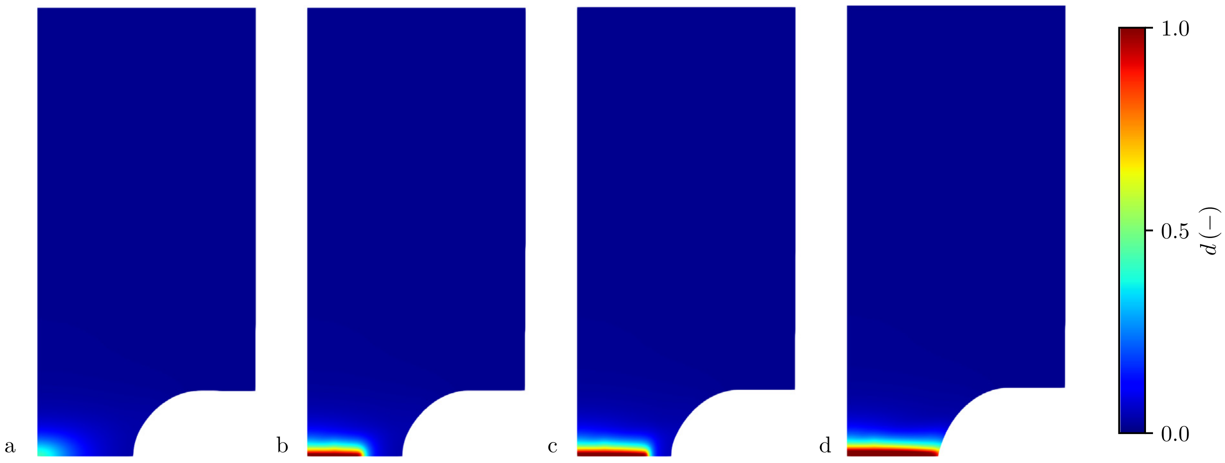

Fig. 9. Evolution of contour plots of the fracture phase field for the specimen with $r_N = 1.59$ mm for the A572 Grade 50 steel at displacements of (a) 0.67 mm, (b) 0.68 mm, (c) 0.72 mm, and (d) 0.83 mm.

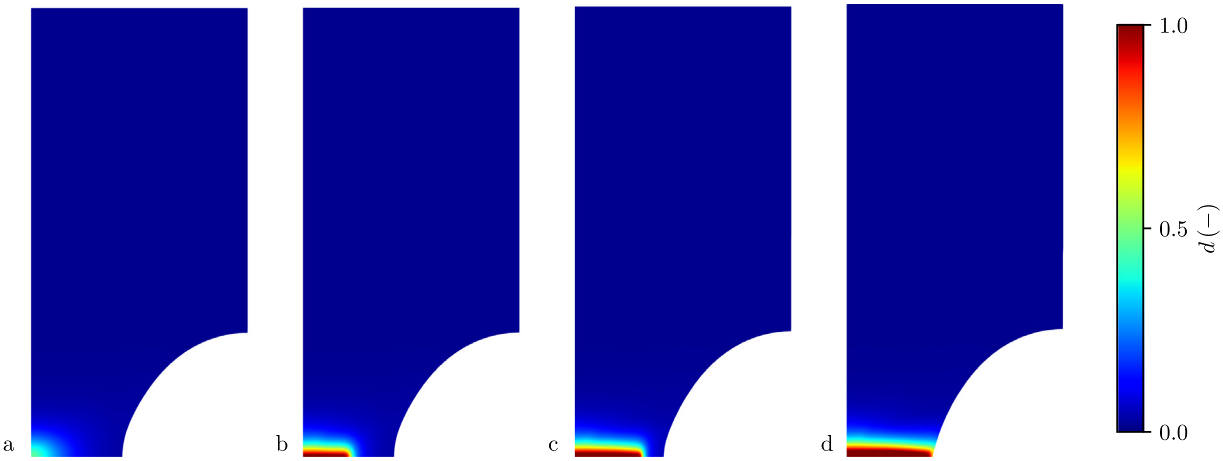

Fig. 10. Evolution of contour plots of the fracture phase field for the specimen with $r_{\mathrm{N}} = 3.18$ mm for the A572 Grade 50 steel at displacements of (a) 0.95 mm, (b) 0.96 mm, (c) 1.03 mm, and (d) 1.16 mm.

Table 3
Dimensions for the GP specimen.

w_{UN} (mm)	h (mm)	t (mm)	w_{NR} (mm)	r_{N} (mm)
9.53	25.4	19.05	2.54	2.03

Table 4
Parameters for the GP test.

E (GPa)	ν (–)	τ_0 (MPa)	Q_∞ (MPa)	b (–)	G_c^0 (N/mm)	$\mathcal{C}$ (–)	$\mathcal{B}$ (–)	$\mathcal{K}$ (–)
205	0.3	240	265	14	85	0.17	0.5	2

5.2. Grooved Plate (GP) test

The CNT tests discussed in the previous section allow for investigating different levels of stress triaxiality. However, they are limited to axisymmetric stress states with $\zeta \approx 1$. To investigate stress states characterized by a Lode angle parameter close to zero at the location of crack initiation, Grooved Plate (GP) tests are used, cf. Fig. 3. Accordingly, for assessing the proposed model, the GP test performed by Terashima and Deierlein [75] on steel of grade A36 is investigated in this example. The geometry of a GP specimen and the loading conditions are visualized in Fig. 11. A specimen for the GP test is characterized by two smooth notches along its depth. As a consequence of the geometry, the stress state in the vicinity of the crack tip is characterized by nearly plane strain conditions. Similar to the CNT tests, the level of stress triaxiality experienced at the crack initiation location can be adjusted by changing the specimen geometry, namely the notch aspect ratio $\frac{r_{\mathrm{N}}}{w_{\mathrm{NR}}}$ [53,75]. The dimensions for the specimen used in the investigated GP test are summarized in Table 3.

For the finite element simulation, the symmetry of the specimen is exploited, and accordingly, only one eighth of the body is modeled. Brick elements with an approximate size of 0.07 mm are used in regions where crack is expected to propagate. For the crack phase field, a length scale parameter of $l = 0.25$ mm is used. The parameters used for this test are listed in Table 4.

Fig. 12a illustrates the obtained load–displacement response where a good agreement with the experimental data is shown. In particular, the pre-peak behavior is captured perfectly by the proposed framework, whereas the load–displacement curve in the early post peak region is slightly underestimated by the model, which however, is mainly attributed to the assumed simplistic form of the plasticity model. For the stage of final rupture, again a perfect agreement, characterized by a virtually identical slope of the load–displacement curve, is observed. Fig. 12b depicts the distribution of the stress triaxiality T and the Lode angle parameter ζ along the thickness of the specimen once

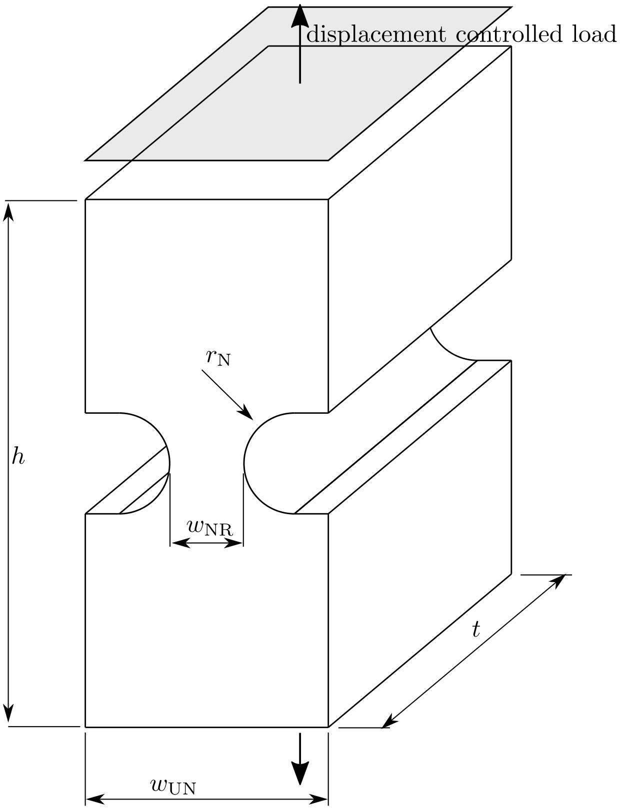

Fig. 11. Geometry of the GP specimen. For the loading, the top and bottom surfaces of the specimen are pulled vertically in a displacement controlled manner.

the crack phase field attains a value of $d = 0.05$, and a macroscopic crack starts to form. A high value of stress triaxiality in combinations with a nearly zero Lode angle parameter are observed at the crack initiation location.

Finally, Figs. 13 and 14, respectively depict the resulting crack patterns and the internal plastic variable for different stages of the test. As apparent, the crack initiates at the center of the specimen, where the stress triaxiality attains a high value, and it propagates in both depth and thickness directions. Interestingly, the evolution of the internal plastic variable shows that α is highest not at the crack initiation location but at the free surface, i.e., the groove tip, of the specimen.

5.3. Blunt Notch (BN) test

The CNT and GP tests studied are characterized by moderate to high level of stress triaxiality as well as $\zeta \approx 1$ and $\zeta \approx 0$, respectively. Therefore, to investigate comparatively low to moderate levels of stress triaxiality, i.e., $T < 1$, combined with Lode angle parameters in the range $0 < \zeta < 1$, Blunt Notch (BN) tests are used. In particular, we investigate a test performed by Ziccarelli [54] on A913 Grade 65 steel. The geometry of the studied BN test specimen alongside the loading conditions are shown in Fig. 15. Similar to the CNT and the GP tests, the stress triaxiality and the Lode angle parameter can be adjusted by modifying the geometry, specifically by changing the notch radius r_N and the horizontal distance between the loading point and the notch tip w_N. The dimensions for the investigated BN specimen are listed in Table 5.

For the finite element simulations, two-fold symmetry is exploited. Accordingly, one fourth of the body is modeled using brick elements with an approximate size of 0.26 mm in those areas where the crack is expected to propagate. For the crack phase field, a length scale parameter of $l = 0.6$ mm is used. The employed parameters for this example are summarized in Table 6.

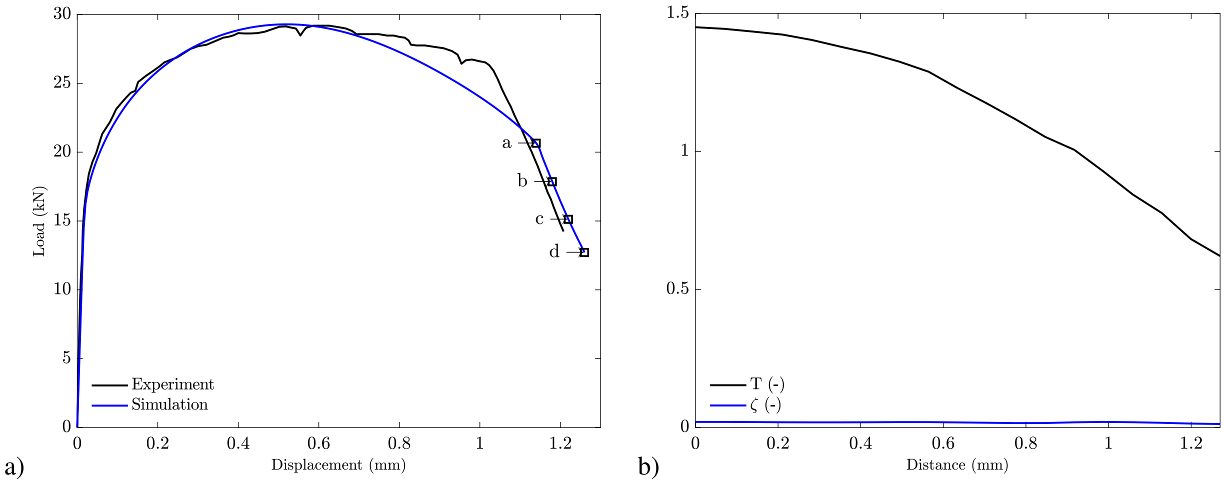

Fig. 12. (a) Computed and experimental (conducted by Terashima and Deierlein [75]) load–displacement curves for the GP test and (b) distribution of the stress triaxiality T and the Lode angle parameter ζ from the center of specimen to the groove tip once $d = 0.05$. Markers shown on the load–displacement curve correspond to the evaluation plots shown in Figs. 13 and 14.

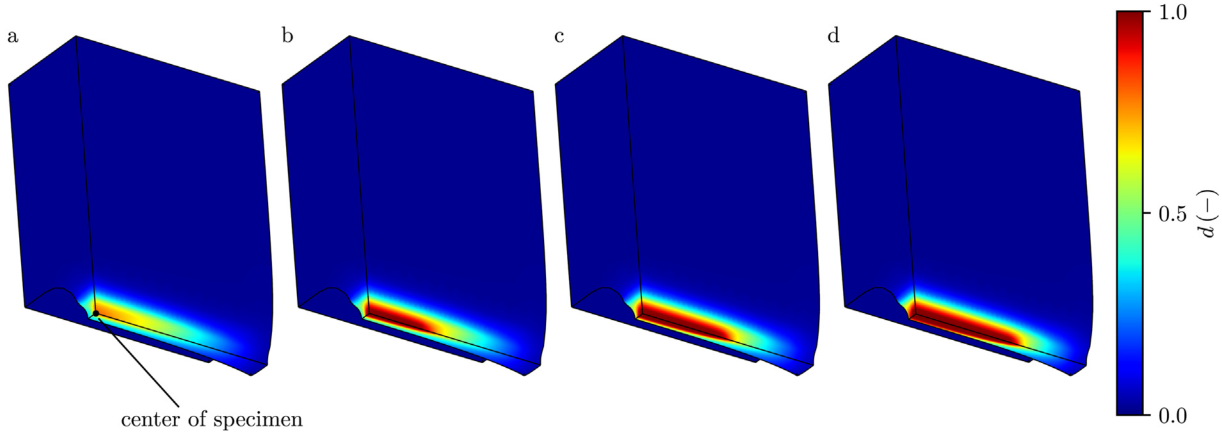

Fig. 13. Evolution of contour plots of the fracture phase field for the GP test at displacements of (a) 1.14 mm, (b) 1.18 mm, (c) 1.22 mm, and (d) 1.26 mm.

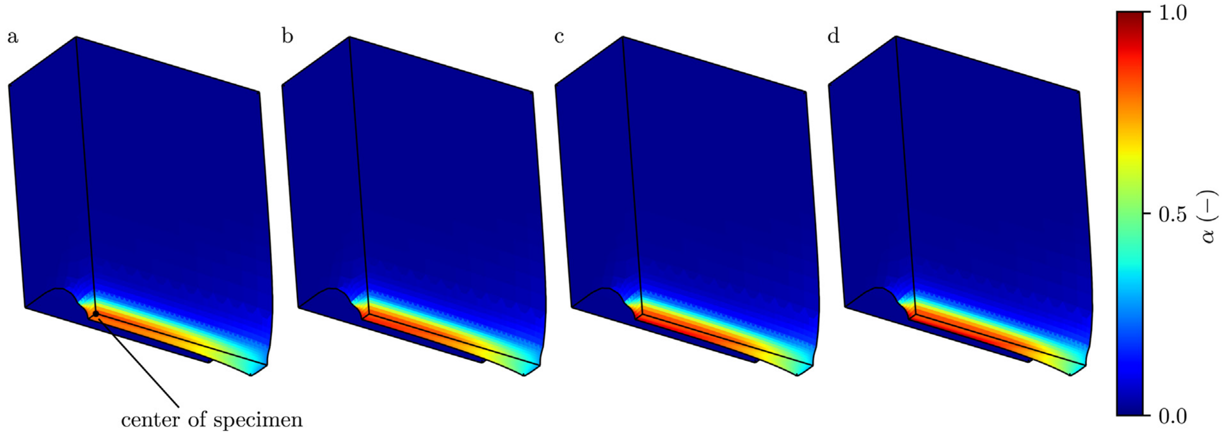

Fig. 14. Evolution of contour plots of the internal plastic variable α for the GP test at displacements of (a) 1.14 mm, (b) 1.18 mm, (c) 1.22 mm, and (d) 1.26 mm.

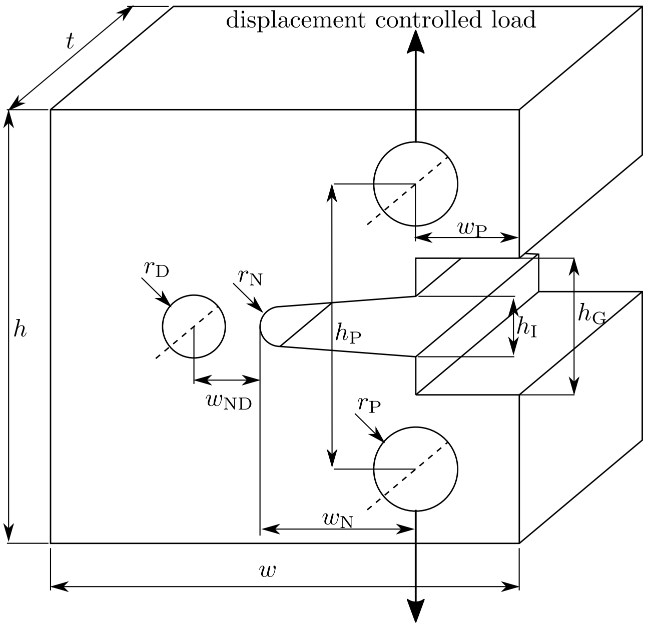

Fig. 15. Geometry of the BN test. For the loading, top and bottom edges of the holes are moved vertically in a displacement controlled manner.

Table 5
Dimensions for the BN test.

w (mm)	h (mm)	t (mm)	w_P (mm)	w_N (mm)	w_{ND} (mm)
63.5	60.96	12.7	12.7	25.4	6.35
h_G (mm)	h_I (mm)	h_P (mm)	r_D (mm)	r_P (mm)	r_N (mm)
12.7	5.08	36.07	1.59	6.35	0.79

Table 6
Parameters for the BN test.

E (GPa)	ν (–)	τ_0 (MPa)	Q_∞ (MPa)	b (–)	G_c^0 (N/mm)	$\mathcal{C}$ (–)	$\mathcal{B}$ (–)	$\mathcal{K}$ (–)
205	0.3	410	245	18	265	0.65	0.5	2

Fig. 16a shows the predicted load–displacement curve together with the experimental data. The considered displacement is taken to be the vertical movement of the holes, as visualized in Fig. 15. A good agreement between the simulated results and the experimental data is stated.

Fig. 16b shows the evolution of the stress triaxiality and the Lode angle parameter at the tip of the notch located on the plane of symmetry until the crack phase field reaches $d = 0.05$. A moderate value of stress triaxiality alongside an intermediate Lode angle parameter are visible.

The evolution of damage in the specimen is visualized in Fig. 17. For this example, the crack initiates at the tip of the notched hole on the plane of symmetry, and then as expected, propagates horizontally and outward towards the free surface and reaches the drilled hole. In this example, unlike the other two examples, the crack does not initiate at the location with the highest level of stress triaxiality, rather it starts from the location where a combination of the stress triaxiality and large plastic deformation leads to crack nucleation. Fig. 18 depicts the distribution of the stress triaxiality and the internal plastic variable when $d \approx 1$ at the notch tip. This demonstrates the capability of the SWDFM in accounting for not only the stress state but also the plastic deformation experienced by material points for predicting different ductile crack mechanisms.

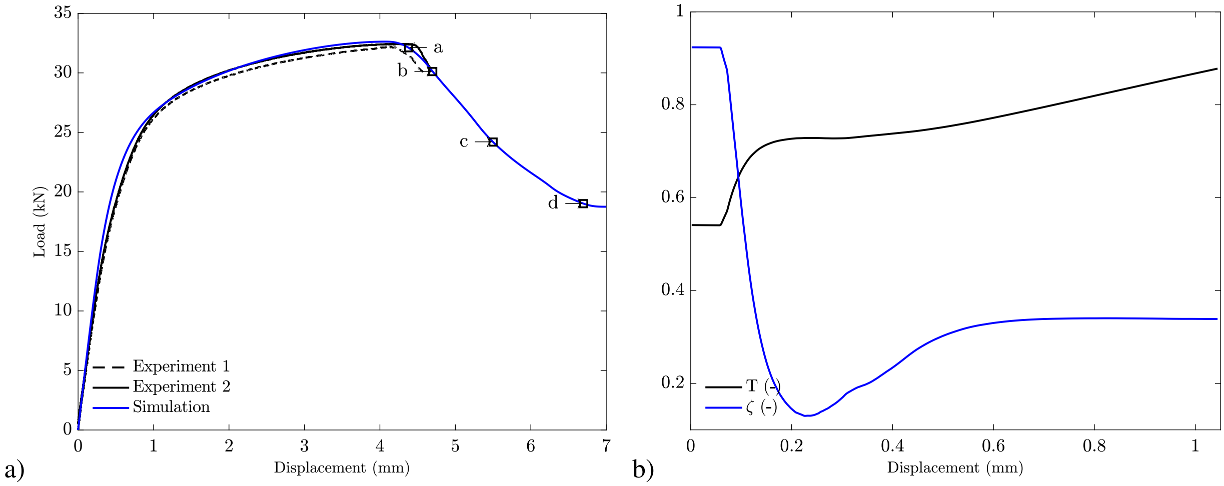

Fig. 16. (a) Computed and experimental (conducted by Ziccarelli [54]) load–displacement curves for the BN test and (b) evolution of the stress triaxiality T, and the Lode angle parameter ζ at the tip of the notch located on the plane of symmetry in the BN specimen until $d = 0.05$ at crack initiation location. Markers shown on the load–displacement curve correspond to the evaluation plots shown in Fig. 17.

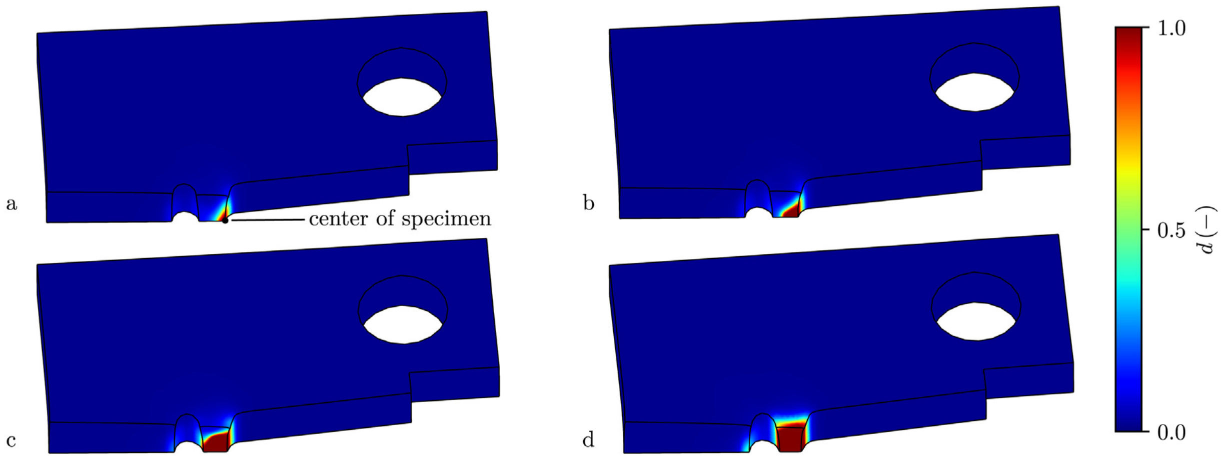

Fig. 17. Evolution of contour plots of the fracture phase field for the BN test at displacements of (a) 4.38 mm, (b) 4.70 mm, (c) 5.50 mm, and (d) 6.70 mm.

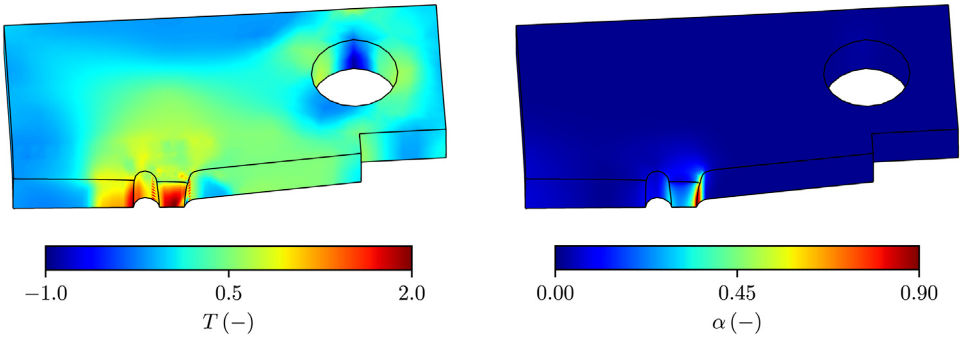

Fig. 18. Distribution of the stress triaxiality T and the internal plastic variable α for the BN test when $d \approx 1$ at the notch tip.

6. Conclusion

In this work, we proposed a phase field framework for predicting crack initiation and propagation in elastoplastic solids experiencing multi-axial stress states under finite, inelastic deformations. To this end, we followed a micromechanically motivated approach for deriving the governing equations, accompanied with the first and second laws of thermodynamics. The proposed framework assumes a close coupling between the history of the material and the evolution of damage through degradation of the fracture toughness. To account for different multi-axial stress states, the degradation of the fracture toughness is coupled with the Stress-Weighted Ductile Fracture Model (SWDFM). This allows for accurately predicting fracture initiation and advancement in solids, while accounting for both plastic deformation and stress state inside the body. To avoid nonphysical elastic deformations in damaged regions, a degradation function for the plastic yield surface is employed. In addition to shrinking the plastic yield surface, this degradation function circumvents numerical difficulties arising from an excessive accumulation of plastic deformation in severely damaged regions. Furthermore, following the second law of thermodynamics, restrictions were enforced on the rate at which the fracture toughness can degrade.

The capabilities of the proposed model were validated in a numerical study covering a wide range of stress and strain states. In particular, the Cylindrical Notched Tension (CNT) test, the Grooved Plate (GP) test and the Blunt Notch (BN) test have been investigated. Special emphasis was put on the comparison with experimental results from real world experiments. Thereby, it was shown that the ductile fracture response observed in different tests are accurately captured by only using a set of material-specific parameters.

Regarding future research endeavors, possible extensions of the proposed model include ductile fracture under cyclic loadings, taking into account kinematic hardening effects. Such extensions are currently pending.

Declaration of competing interest

The authors declare that they have no known competing financial interests or personal relationships that could have appeared to influence the work reported in this paper.

Data availability

Data will be made available on request.

Acknowledgments

Financial support for this research was provided by the Department of Energy, National Nuclear Security Administration, Predictive Science Academic Alliance Program (PSAAP), USA under Award Number DE-NA0003962, the National Science Foundation, USA through grants CMMI-1911836 and CMMI-1635043, the John A. Blume Earthquake Engineering Center at Stanford University, USA, and the Max Kade Foundation (New York), USA through the Max Kade Fellowship Program. This support is gratefully acknowledged.

References

[1] A.A. Griffith, The phenomena of rupture and flow in solids, Philos. Trans. R. Soc. Lond. A 221 (582–593) (1921) 163–198.

[2] G.A. Francfort, J.-J. Marigo, Revisiting brittle fracture as an energy minimization problem, J. Mech. Phys. Solids 46 (8) (1998) 1319–1342.

[3] B. Bourdin, G. Francfort, J.-J. Marigo, Numerical experiments in revisited brittle fracture, J. Mech. Phys. Solids 48 (4) (2000) 797–826.

[4] N. Moës, J. Dolbow, T. Belytschko, A finite element method for crack growth without remeshing, Internat. J. Numer. Methods Engrg. 46 (1) (1999) 131–150.

[5] C. Linder, F. Armero, Finite elements with embedded strong discontinuities for the modeling of failure in solids, Internat. J. Numer. Methods Engrg. 72 (12) (2007) 1391–1433.

[6] F. Armero, C. Linder, New finite elements with embedded strong discontinuities in the finite deformation range, Comput. Methods Appl. Mech. Engrg. 197 (2008) 3138–3170.

[7] F. Armero, J. Kim, Three-dimensional finite elements with embedded strong discontinuities to model material failure in the infinitesimal range, Internat. J. Numer. Methods Engrg. 91 (2012) 1291–1330.

[8] C. Linder, A. Raina, A strong discontinuity approach on multiple levels to model solids at failure, Comput. Methods Appl. Mech. Engrg. 253 (2013) 558–583.

[9] C. Linder, X. Zhang, A marching cubes based failure surface propagation concept for three-dimensional finite elements with non-planar embedded strong discontinuities of higher-order kinematics, Internat. J. Numer. Methods Engrg. 96 (2013) 339–372.

[10] C. Miehe, F. Welschinger, M. Hofacker, Thermodynamically consistent phase-field models of fracture: Variational principles and multi-field FE implementations, Internat. J. Numer. Methods Engrg. 83 (10) (2010) 1273–1311.

[11] C. Miehe, M. Hofacker, F. Welschinger, A phase field model for rate-independent crack propagation: Robust algorithmic implementation based on operator splits, Comput. Methods Appl. Mech. Engrg. 199 (45–48) (2010) 2765–2778.

[12] H. Amor, J.-J. Marigo, C. Maurini, Regularized formulation of the variational brittle fracture with unilateral contact: Numerical experiments, J. Mech. Phys. Solids 57 (8) (2009) 1209–1229.

[13] M.J. Borden, C.V. Verhoosel, M.A. Scott, T.J. Hughes, C.M. Landis, A phase-field description of dynamic brittle fracture, Comput. Methods Appl. Mech. Engrg. 217–220 (2012) 77–95.

[14] B. Bourdin, C.J. Larsen, C.L. Richardson, A time-discrete model for dynamic fracture based on crack regularization, Int. J. Fract. 168 (2) (2011) 133–143.

[15] J.-F. Remacle, J. Lambrechts, B. Seny, E. Marchandise, A. Johnen, C. Geuzainet, Blossom-Quad: A non-uniform quadrilateral mesh generator using a minimum-cost perfect-matching algorithm, Internat. J. Numer. Methods Engrg. 89 (9) (2012) 1102–1119.

[16] R.J. Geelen, Y. Liu, T. Hu, M.R. Tupek, J.E. Dolbow, A phase-field formulation for dynamic cohesive fracture, Comput. Methods Appl. Mech. Engrg. 348 (2019) 680–711.

[17] C. Miehe, L.-M. Schänzel, Phase field modeling of fracture in rubbery polymers. Part I: Finite elasticity coupled with brittle failure, J. Mech. Phys. Solids 65 (2014) 93–113.

[18] B. Talamini, Y. Mao, L. Anand, Progressive damage and rupture in polymers, J. Mech. Phys. Solids 111 (2018) 434–457.

[19] S. Swamynathan, S. Jobst, D. Kienle, M.-A. Keip, Phase-field modeling of fracture in strain-hardening elastomers: Variational formulation, multiaxial experiments and validation, Eng. Fract. Mech. 265 (2022) 108303.

[20] J. Reinoso, M. Paggi, C. Linder, Phase field modeling of brittle fracture for enhanced assumed strain shells at large deformations: formulation and finite element implementation, Comput. Mech. 59 (6) (2017) 981–1001.

[21] J. Kiendl, M. Ambati, L. De Lorenzis, H. Gomez, A. Reali, Phase-field description of brittle fracture in plates and shells, Comput. Methods Appl. Mech. Engrg. 312 (2016) 374–394, Phase Field Approaches to Fracture.

[22] J. Choo, W. Sun, Coupled phase-field and plasticity modeling of geological materials: From brittle fracture to ductile flow, Comput. Methods Appl. Mech. Engrg. 330 (2018) 1–32.

[23] S. Zhou, X. Zhuang, T. Rabczuk, Phase field modeling of brittle compressive-shear fractures in rock-like materials: A new driving force and a hybrid formulation, Comput. Methods Appl. Mech. Engrg. 355 (2019) 729–752.

[24] X. Zhang, A. Krischok, C. Linder, A variational framework to model diffusion induced large plastic deformation and phase field fracture during initial two-phase lithiation of silicon electrodes, Comput. Methods Appl. Mech. Engrg. 312 (2016) 51–77.

[25] P. Cheng, H. Zhu, Y. Zhang, Y. Jiao, J. Fish, Coupled thermo-hydro-mechanical-phase field modeling for fire-induced spalling in concrete, Comput. Methods Appl. Mech. Engrg. 389 (2022) 114327.

[26] J.-Y. Wu, V.P. Nguyen, C.T. Nguyen, D. Sutula, S. Sinaie, S.P. Bordas, in: S.P. Bordas, D.S. Balint (Eds.), Chapter One - Phase-Field Modeling of Fracture, in: Advances in Applied Mechanics, vol. 53, Elsevier, 2020, pp. 1–183.

[27] M.J. Borden, T.J. Hughes, C.M. Landis, A. Anvari, I.J. Lee, A phase-field formulation for fracture in ductile materials: Finite deformation balance law derivation, plastic degradation, and stress triaxiality effects, Comput. Methods Appl. Mech. Engrg. 312 (2016) 130–166.

[28] C. Li, J. Fang, C. Wu, G. Sun, G. Steven, Q. Li, Phase field fracture in elasto-plastic solids: Incorporating phenomenological failure criteria for ductile materials, Comput. Methods Appl. Mech. Engrg. 391 (2022) 114580.

[29] M. Ambati, T. Gerasimov, L. De Lorenzis, Phase-field modeling of ductile fracture, Comput. Mech. 55 (5) (2015) 1017–1040.

[30] M. Ambati, R. Kruse, L. De Lorenzis, A phase-field model for ductile fracture at finite strains and its experimental verification, Comput. Mech. 57 (1) (2016) 149–167.

[31] B. Yin, M. Kaliske, A ductile phase-field model based on degrading the fracture toughness: Theory and implementation at small strain, Comput. Methods Appl. Mech. Engrg. 366 (2020) 113068.

[32] J. Han, S. Matsubara, S. Moriguchi, M. Kaliske, K. Terada, Crack phase-field model equipped with plastic driving force and degrading fracture toughness for ductile fracture simulation, Comput. Mech. 69 (1) (2021) 151–175.

[33] R. Alessi, M. Ambati, T. Gerasimov, S. Vidoli, L. De Lorenzis, Comparison of phase-field models of fracture coupled with plasticity, in: Advances in Computational Plasticity: A Book in Honour of D. Roger J. Owen, Springer International Publishing, Cham, 2018, pp. 1–21.

[34] C. Miehe, M. Hofacker, L.-M. Schänzel, F. Aldakheel, Phase field modeling of fracture in multi-physics problems. Part II. Coupled brittle-to-ductile failure criteria and crack propagation in thermo-elastic–plastic solids, Comput. Methods Appl. Mech. Engrg. 294 (2015) 486–522.

[35] F. Aldakheel, P. Wriggers, C. Miehe, A modified Gurson-type plasticity model at finite strains: formulation, numerical analysis and phase-field coupling, Comput. Mech. 62 (4) (2018) 815–833.

[36] V. Tvergaard, A. Needleman, Analysis of the cup-cone fracture in a round tensile bar, Acta Metall. 32 (1) (1984) 157–169.

[37] V. Tvergaard, On localization in ductile materials containing spherical voids, Int. J. Fract. 18 (4) (1982) 237–252.

[38] F.A. McClintock, A criterion for ductile fracture by the growth of holes, J. Appl. Mech. 35 (2) (1968) 363–371.

[39] J. Rice, D. Tracey, On the ductile enlargement of voids in triaxial stress fields, J. Mech. Phys. Solids 17 (3) (1969) 201–217.

[40] J. Lemaitre, A continuous damage mechanics model for ductile fracture, J. Eng. Mater. Technol. 107 (1) (1985) 83–89.

[41] G. La Rosa, G. Mirone, A. Risitano, Effect of stress triaxiality corrected plastic flow on ductile damage evolution in the framework of continuum damage mechanics, Eng. Fract. Mech. 68 (4) (2001) 417–434.

[42] D.M. Norris Jr., J.E. Reaugh, B. Moran, D.F. Quiñones, A plastic-strain, mean-stress criterion for ductile fracture, J. Eng. Mater. Technol. 100 (3) (1978) 279–286.

[43] M. Oyane, T. Sato, K. Okimoto, S. Shima, Criteria for ductile fracture and their applications, J. Mech. Work. Technol. 4 (1) (1980) 65–81.

[44] Y. Bao, T. Wierzbicki, On fracture locus in the equivalent strain and stress triaxiality space, Int. J. Mech. Sci. 46 (1) (2004) 81–98.
[45] D. Chu, X. Li, Z. Liu, J. Cheng, T. Wang, Z. Li, Z. Zhuang, A unified phase field damage model for modeling the brittle-ductile dynamic failure mode transition in metals, Eng. Fract. Mech. 212 (2019) 197–209.
[46] H. Li, M. Fu, J. Lu, H. Yang, Ductile fracture: Experiments and computations, Int. J. Plast. 27 (2) (2011) 147–180.
[47] H. Li, M. Fu, Chapter 3 - Damage evolution and ductile fracture, in: H. Li, M. Fu (Eds.), Deformation-Based Processing of Materials, Elsevier, 2019, pp. 85–136.
[48] M. Neuner, P. Gamnitzer, G. Hofstetter, A 3D gradient-enhanced micropolar damage-plasticity approach for modeling quasi-brittle failure of cohesive-frictional materials, Comput. Struct. 239 (2020) 106332.
[49] M. Neuner, R. Regueiro, C. Linder, A unified finite strain gradient-enhanced micropolar continuum approach for modeling quasi-brittle failure of cohesive-frictional materials, Int. J. Solids Struct. (2022) 111841.
[50] G.R. Johnson, W.H. Cook, Fracture characteristics of three metals subjected to various strains, strain rates, temperatures and pressures, Eng. Fract. Mech. 21 (1) (1985) 31–48.
[51] A.L. Gurson, Continuum theory of ductile rupture by void nucleation and growth: Part I—Yield criteria and flow rules for porous ductile media, J. Eng. Mater. Technol. 99 (1) (1977) 2–15.
[52] C.M. Smith, A.M. Kanvinde, G.G. Deierlein, A Stress-Weighted Damage Model for Ductile Fracture Initiation in Structural Steel under Cyclic Loading and Generalized Stress States, Stanford University, Blume Center, Stanford, CA, 2014, pp. 1–335.
[53] C. Smith, A. Ziccarelli, M. Terashima, A. Kanvinde, G. Deierlein, A stress-weighted ductile fracture model for steel subjected to Ultra Low Cycle Fatigue, Eng. Struct. 245 (2021) 112964.
[54] A.J. Ziccarelli, Simulating Earthquake-Induced Ductile Crack Propagation and Brittle Fracture in Steel Structures, Stanford University, 2021.
[55] M. Dittmann, F. Aldakheel, J. Schulte, P. Wriggers, C. Hesch, Variational phase-field formulation of non-linear ductile fracture, Comput. Methods Appl. Mech. Engrg. 342 (2018) 71–94.
[56] T. Hu, B. Talamini, A.J. Stershic, M.R. Tupek, J.E. Dolbow, A variational phase-field model for ductile fracture with coalescence dissipation, Comput. Mech. 68 (2) (2021) 311–335.
[57] E.H. Lee, Elastic-plastic deformation at finite strains, J. Appl. Mech. 36 (1) (1969) 1–6.
[58] J. Mandel, Foundations of Continuum Thermodynamics, Chapter Thermodynamics and Plasticity, MacMillan, London, 1974.
[59] A. Schluter, A. Willenbucher, C. Kuhn, R. Muller, Phase field approximation of dynamic brittle fracture, Comput. Mech. 54 (5) (2014) 1141–1161.
[60] B. Bourdin, G.A. Francfort, J.-J. Marigo, The variational approach to fracture, J. Elasticity 91 (1–3) (2008) 5–148.
[61] J.-Y. Wu, A unified phase-field theory for the mechanics of damage and quasi-brittle failure, J. Mech. Phys. Solids 103 (2017) 72–99.
[62] M.J. Borden, T.J. Hughes, C.M. Landis, C.V. Verhoosel, A higher-order phase-field model for brittle fracture: Formulation and analysis within the isogeometric analysis framework, Comput. Methods Appl. Mech. Engrg. 273 (2014) 100–118.
[63] M.E. Gurtin, Generalized Ginzburg-Landau and Cahn-Hilliard equations based on a microforce balance, Physica D 92 (3) (1996) 178–192.
[64] H. Stumpf, K. Hackl, Micromechanical concept for the analysis of damage evolution in thermo-viscoelastic and quasi-brittle materials, Int. J. Solids Struct. 40 (6) (2003) 1567–1584.
[65] B.D. Coleman, W. Noll, The thermodynamics of elastic materials with heat conduction and viscosity, Arch. Ration. Mech. Anal. 13 (1963) 167–178.
[66] E.A.d.S. Neto, D. Perić, D. Owens, Computational Methods for Plasticity, Wiley, 2008.
[67] T. Linse, P. Hennig, M. Kästner, R. de Borst, A convergence study of phase-field models for brittle fracture, Eng. Fract. Mech. 184 (2017) 307–318.
[68] C. Steinke, M. Kaliske, A phase-field crack model based on directional stress decomposition, Comput. Mech. 63 (5) (2018) 1019–1046.
[69] B. Bourdin, C.J. Larsen, C.L. Richardson, A time-discrete model for dynamic fracture based on crack regularization, Int. J. Fract. 168 (2) (2010) 133–143.
[70] P. Carrara, M. Ambati, R. Alessi, L. De Lorenzis, A framework to model the fatigue behavior of brittle materials based on a variational phase-field approach, Comput. Methods Appl. Mech. Engrg. 361 (2020) 112731.
[71] C. Huang, X. Gao, Development of a phase field method for modeling brittle and ductile fracture, Comput. Mater. Sci. 169 (2019) 109089.
[72] Y.F. Dafalias, Plastic spin: necessity or redundancy? Int. J. Plast. 14 (9) (1998) 909–931.
[73] K. Hashiguchi, Nonlinear Continuum Mechanics for Finite Elasticity-Plasticity, Elsevier, 2020.
[74] A.M. Kanvinde, G.G. Deierlein, Micromechanical Simulation of Earthquake-Induced Fracture in Steel Structures, Blume Center TR 145, Stanford University, 2004.
[75] M. Terashima, G.G. Deierlein, Ductile Fracture Simulation and Risk Quantification of Buckling-Restrained Braces under Earthquakes, Blume Center TR 206, Stanford University, 2018.
[76] S.J. Benson, T.S. Munson, Flexible complementarity solvers for large-scale applications, Optim. Methods Softw. 21 (1) (2006) 155–168.
[77] H. Eldahshan, P.-O. Bouchard, J. Alves, E. Perchat, D.P. Munoz, Phase field modeling of ductile fracture at large plastic strains using adaptive isotropic remeshing, Comput. Mech. 67 (3) (2021) 763–783.
[78] C. Miehe, S. Teichtmeister, F. Aldakheel, Phase-field modelling of ductile fracture: a variational gradient-extended plasticity-damage theory and its micromorphic regularization, Phil. Trans. R. Soc. A 374 (2066) (2016) 20150170.
[79] C. Miehe, F. Aldakheel, S. Teichtmeister, Phase-field modeling of ductile fracture at finite strains: A robust variational-based numerical implementation of a gradient-extended theory by micromorphic regularization, Internat. J. Numer. Methods Engrg. 111 (9) (2017) 816–863.

[80] T. Hu, RACCOON, 2022, URL: https://github.com/hugary1995/raccoon.

[81] T. Hu, RACCOON documentation, 2022, URL: https://hugary1995.github.io/raccoon.

[82] T. Hu, J. Guilleminot, J.E. Dolbow, A phase-field model of fracture with frictionless contact and random fracture properties: Application to thin-film fracture and soil desiccation, Comput. Methods Appl. Mech. Engrg. 368 (2020) 113106.

[83] C.J. Permann, D.R. Gaston, D. Andrš, R.W. Carlsen, F. Kong, A.D. Lindsay, J.M. Miller, J.W. Peterson, A.E. Slaughter, R.H. Stogner, R.C. Martineau, MOOSE: Enabling massively parallel multiphysics simulation, SoftwareX 11 (2020) 100430.

[84] C. Miehe, L.-M. Schänzel, Phase field modeling of fracture in rubbery polymers. Part I: Finite elasticity coupled with brittle failure, J. Mech. Phys. Solids 65 (2014) 93–113.

[85] V. Pericoli, X. Lao, A. Ziccarelli, A. Kanvinde, G. Deierlein, Integration of an adaptive cohesive zone and continuum ductile fracture model to simulate crack propagation in steel structures, Eng. Fract. Mech. 258 (2021) 108041.

[86] H.S. Suh, W.C. Sun, D.T. O'Connor, A phase field model for cohesive fracture in micropolar continua, Comput. Methods Appl. Mech. Engrg. 369 (2020) 113181.